Symmetric stiffness matrices for isoparametric finite elements in nonlinear elasticity

Paolo S. Valvo[1,2]

Abstract
The article illustrates a position-based finite element formulation, which greatly simplifies the statement of nonlinear elasticity problems. The formulation adopts as main unknowns the nodal positions in the current configuration instead of the nodal displacements. As a result, simple analytical expressions are obtained of the secant and tangent stiffness matrices for general isoparametric finite elements. Contrary to most formulations of the literature, the secant stiffness matrices turn out to be symmetric. Furthermore, any hyperelastic constitutive law can be easily implemented. Specialised expressions are deduced for the stiffness matrices of a two-node truss bar element and a three-node planar triangular element. The validity of the proposed approach is illustrated through the analysis of a steep von Mises truss and Cook's membrane. For illustration, the de Saint Venant–Kirchhoff and neo-Hookean material models are considered.

Keywords Finite element method · Isoparametric element · Stiffness matrix · Nonlinear elasticity · Symmetry

Mathematics Subject Classification 74B20 · 74K10 · 74K15 · 74S05

1 Introduction

1.1 Motivation

In the finite element method (FEM) [1], the linear static equilibrium equations can be written in the following form:

$$\mathbf{K}\mathbf{u} = \mathbf{p} + \mathbf{r}, \tag{1}$$

where $\mathbf{u}, \mathbf{p}$, and $\mathbf{r} \in \mathbb{R}^N$ are the vectors of (generalised) nodal displacements, loads, and restraint reactions, respectively; $\mathbf{K} \in \mathbb{R}^{N \times N}$ is the symmetric and positive-definite stiffness matrix; N is the number of degrees of freedom (DOFs) of the model.

In the standard displacement-based finite element formulation (DFEF), the nodal displacement vector, $\mathbf{u}$, is the main unknown. In the solution procedure, first, Eq. (1)—together with the kinematic restraint equations, if present—are solved with respect to $\mathbf{u}$. Then, the nodal restraint reaction vector, $\mathbf{r}$, is calculated.

In a total Lagrangian formulation [2, 3], the nonlinear static equilibrium equations can be written in a form similar to Eq. (1),

$$\mathbf{K}(\mathbf{u})\mathbf{u} = \mathbf{p} + \mathbf{r}, \tag{2}$$

where $\mathbf{K}(\mathbf{u})$ is the secant stiffness matrix that now depends on $\mathbf{u}$. Because of nonlinearity, Eq. (2) have to be solved by using some incremental and/or iterative method. The incremental, or updated Lagrangian, formulation requires the introduction of the tangent stiffness matrix, $\mathbf{K}_T(\mathbf{u}) = \partial[\mathbf{K}(\mathbf{u})\mathbf{u}]/\partial\mathbf{u}$. In this respect, it is worth noting that while the tangent stiffness matrix, $\mathbf{K}_T(\mathbf{u})$, is always symmetric, the secant stiffness matrix, $\mathbf{K}(\mathbf{u})$, is in general unsymmetric—which is undesirable from the computational point of view. Moreover, the secant stiffness matrix has no unique repre-

✉ Paolo S. Valvo
p.valvo@ing.unipi.it

1 Department of Civil and Industrial Engineering, University of Pisa, Largo Lucio Lazzarino, 56122 Pisa, PI, Italy

2 Gruppo Nazionale per la Fisica Matematica (GNFM), Istituto Nazionale di Alta Matematica (INdAM) "Francesco Severi", P.le Aldo Moro, 5, 00185 Roma, Italy

sentation: indeed, several alternative expressions are possible that yield the same result for the elastic force vector, $\mathbf{f}(\mathbf{u}) = \mathbf{K}(\mathbf{u})\mathbf{u}$. Such circumstances stimulated a number of studies aimed at obtaining simple, possibly symmetric, expressions of the secant stiffness matrix. For a historical survey on early developments, the interested reader is referred to the works by Felippa et al. [4] and Oñate [5].

Oñate [5] used the principle of virtual work (PVW) to deduce a general parametric expression of the secant stiffness matrix for three-dimensional (3D) isoparametric elements and specialised expressions for truss bar elements. In general, the obtained secant stiffness matrices are not symmetric, but become symmetric for a particular choice of the parameters. A linear relationship is assumed between the Green–Lagrange strain and second Piola–Kirchhoff stress tensors. Hence, strictly speaking, the proposed formulation is valid only for the de Saint Venant–Kirchhoff (SVK) material model. However, it can be used also for other nonlinear hyperelastic materials in incremental form.

Morán et al. [6] applied the principle of stationary total potential energy (TPE) to deduce symmetric expressions of the secant stiffness matrix under the assumption that the strain energy density can be decomposed into a set of homogeneous functions. As an example, they derived the expressions for a two-dimensional (2D) Euler–Bernoulli beam element.

Pedersen [7] determined analytical expressions of the secant stiffness matrix for 2D triangular elements in plane elasticity problems. He considered both linear and nonlinear power-law stress–strain relationships. Also, he extended the same formulation to tetrahedral elements in 3D elasticity problems [8]. Later, Gülümser et al. [9] proposed a faster implementation of Pedersen's method for tetrahedral elements. The obtained secant stiffness matrices are generally unsymmetric.

As a matter of fact, if arbitrary hyperelastic constitutive laws are assumed, the secant stiffness matrices obtained within the standard DFEF turn out to be unsymmetric. Moreover, their analytical expressions may be complicated and cumbersome to implement, except for a few special cases (see Appendix A). Therefore, in the literature, the explicit derivation of the secant stiffness matrix is often avoided and the nonlinear elastic force vector, $\mathbf{f}(\mathbf{u})$, is assembled directly from the elemental contributions [2].

1.2 Main idea

This paper illustrates a method for the derivation of symmetric secant stiffness matrices for general isoparametric elements with arbitrary hyperelastic constitutive law. The formulation can be used for both 2D and 3D nonlinear elasticity problems. The obtained expressions are simple and easy to implement in a software code. The key to achieve such results is to adopt a position-based finite element formula-

tion (PFEF). Accordingly, the vector of nodal positions in the current configuration, $\mathbf{x} \in \mathbb{R}^N$, is chosen as the main unknown instead of the nodal displacement vector, $\mathbf{u}$. With this choice, the nonlinear static equilibrium Eq. (2) can be rewritten as follows:

$$\mathbf{S}(\mathbf{x})\mathbf{x} = \mathbf{p} + \mathbf{r}, \tag{3}$$

where $\mathbf{S}(\mathbf{x}) \in \mathbb{R}^{N \times N}$ is the secant stiffness matrix referred to the nodal position vector. As will be detailed in the following, this secant stiffness matrix turns out to be always symmetric [10].

1.3 Comparison with similar approaches

To the best of the Author's knowledge, Bonet [11] was the first to propose using the nodal positions instead of the nodal displacements in the implementation of Newton–Raphson's iterative method for the finite element simulation of plastic flow. Later, Bonet et al. [12] successfully extended this approach to the analysis of inflated membranes, as well as to the nonlinear static and dynamic analysis of hyperelastic solids undergoing large displacements and strains [13, 14].

The PFEF was independently adopted by Coda and Greco [15] for the large displacement analysis of 2D frames. Then, the same research group applied this formulation to the elasto-plastic analysis of space trusses [16], the dynamic analysis of flexible multi-body systems [17], and the geometrically nonlinear analysis of shells [18]. In all of such early papers, linearly elastic material behaviour is assumed. In more recent contributions, the PFEF is applied to the analysis of elasto-plastic and hyperelastic solids [19], incompressible fluids [20], and multiscale materials [21].

The PFEF turns out to be similar to the absolute nodal coordinate formulation (ANCF) introduced by Shabana [22, 23] in the context of flexible multibody dynamics. In the ANCF, the nodal coordinates and their derivatives with respect to a global Cartesian reference system are assumed as main unknowns. This formulation was originally introduced for beam elements, and later extended to plates and shells [24, 25]. Apparently, less efforts have been devoted to the development of finite elements for the discretisation of general continuous bodies [26, 27]. Most studies adopting the ANCF assume linearly elastic material behaviour in line with the SVK material model. Few contributions consider more general nonlinear hyperelastic materials: also in this case, most studies focus on beam elements [28]. Orzechowski and Frączeks [29] developed an ANCF straight beam element made of incompressible neo-Hookean (NH) or Mooney-Rivlin (MR) material. Obrezkov et al. [30] formulated an ANCF straight beam element with three alternative nonlinear hyperelastic constitutive laws: namely, the NH, MR, and Gasser-Ogden-Holzapfel (GOH) material models. Recently,

Li et al. [31] developed an ANCF curved beam element made of incompressible NH material. Luo et al. [32] formulated ANCF shell elements considering both the NH and MR material models. In the ANCF, emphasis is on dynamic problems. Thus, special attention is paid to the formulation of the mass matrix, which turns out to be constant and lacking of terms depending on centrifugal and Coriolis forces.

In all of the above-mentioned studies on the PFEF and ANCF, the secant stiffness matrix is not determined explicitly and the internal force vector is directly assembled from the elemental contributions. A notable exception is the work by García-Vallejo et al. [33], who deduced an explicit expression of the symmetric secant stiffness matrix for an ANCF beam element made of linearly elastic material.

Lastly, it should be mentioned that symmetric stiffness matrices depending on the nodal positions were obtained by Pauletti [34] in the formulation of the natural force density method (NFDM) for the form finding of taut structures. The method was first presented for cable and triangular membrane elements [35], and later extended to quadrilateral [36] and tetrahedral elements [37]. The NFDM stiffness matrices depend on the force densities, which are related to the second Piola–Kirchhoff stress. However, no constitutive laws are explicitly introduced as the NFDM is used only for form finding and not for nonlinear structural analysis.

1.4 Paper organisation

This paper is organised as follows. In Sect. 2, first, the theoretical framework is outlined of the position-based finite element formulation. Then, analytical expressions are deduced of the secant and tangent stiffness matrices for general isoparametric elements. The nonlinear static equilibrium equations are derived from the principle of stationary total potential energy. In Sect. 3, the general expressions of the secant and tangent stiffness matrices are specialised for a two-node truss bar element and a three-node planar triangular element with linear shape functions. In Sect. 4, the effectiveness of the proposed approach is illustrated through the analysis of two benchmark problems: a steep von Mises truss and Cook's membrane. Next, in Sect. 5, the strengths and weaknesses of the proposed formulation are discussed, also with reference to computational performances. Lastly, in Sect. 6, some possible future developments are briefly outlined.

2 Theoretical formulation

2.1 Finite element discretisation

Let us consider a continuous solid body, $\mathcal{B}$, occupying a configuration, Ω (here, regarded as a bounded and connected region), in the Euclidean space, $\mathcal{E}$. The dimension of the space is denoted by $d \in \{1, 2, 3\}$. Let us fix a global Cartesian reference system, $O x_1 \ldots x_d$. The unit vectors of the reference axes are denoted $\mathbf{e}_1, \ldots, \mathbf{e}_d$.

In the finite element (FE) model, the region Ω is approximated by the union of m regions, Ω_e (with $e = 1, \ldots, m$), corresponding to the finite elements (Fig. 1). Elements interact with each other and the surroundings only at a discrete set of points, $K_1, \ldots, K_n$, called nodes. All of the material properties of the continuous body, as well as the distributed forces and kinematic restraints, are modelled as lumped nodal entities in the discrete FE model [1, 2].

Let $\mathbf{x}_j = K_j - O \in \mathbb{R}^d$ be the position vector of the j-th node (with $j = 1, \ldots, n$). The position vectors of all the nodes of the model are collected into the global position vector, $\mathbf{x} = [\mathbf{x}_1; \ldots; \mathbf{x}_n] \in \mathbb{R}^{nd}$.

Among the many configurations that the body can occupy, a particular one, $\bar{\Omega}$, is chosen as the reference configuration. Here, let $\bar{K}_1, \ldots, \bar{K}_n$ be the points corresponding to the node positions. Consistently, $\bar{\mathbf{x}}_j = \bar{K}_j - O \in \mathbb{R}^d$ denotes the reference position vector of the j-th node and $\bar{\mathbf{x}} = [\bar{\mathbf{x}}_1; \ldots; \bar{\mathbf{x}}_n] \in \mathbb{R}^{nd}$ collects the reference position vectors of all the nodes of the model. Displacements and strains are measured starting from the reference configuration. Thus, by definition, the reference configuration is undeformed. In what follows, it will also be assumed to be stress-free.

The displacement vector of the j-th node is defined as $\mathbf{u}_j = K_j - \bar{K}_j = \mathbf{x}_j - \bar{\mathbf{x}}_j \in \mathbb{R}^d$. The displacement vectors of all the nodes of the model are collected into the global displacement vector, $\mathbf{u} = [\mathbf{u}_1; \ldots; \mathbf{u}_n] \in \mathbb{R}^{nd}$. In the standard FE formulation, $\mathbf{u}$ is assumed as the main unknown. Here, the problem will be alternatively formulated in terms of the global nodal position vector, $\mathbf{x} = \bar{\mathbf{x}} + \mathbf{u}$, in the current configuration [10].

2.2 Isoparametric elements

Let us consider a general finite element of dimension $d_e \leq d$. The element has n_e nodes, whose indices are denoted $j_1^e, \ldots, j_{n_e}^e$ in the global node numbering of the model. The position vectors of all the nodes of the element are collected into the elemental nodal position vector, $\mathbf{x}_e = \left[\mathbf{x}_{j_1^e}; \ldots; \mathbf{x}_{j_{n_e}^e}\right] \in \mathbb{R}^{n_e d}$.

The region, Ω_e, occupied by the element in a configuration is assumed to be the image of a regular domain, $\hat{\Omega}_e \subset \mathbb{R}^{d_e}$, called the parent element, under a smooth invertible mapping, $\phi : \hat{\Omega}_e \to \Omega_e$ (Fig. 2). Each point in the parent element, $\hat{P} \in \hat{\Omega}_e$, is mapped onto a point, $P = \phi(\hat{P}) \in \Omega_e$. The geometry of the parent element is described with respect to a system of dimensionless natural coordinates, $\xi_1, \ldots, \xi_{d_e}$. Let $\boldsymbol{\xi} = \left[\xi_1; \ldots; \xi_{d_e}\right] \in \mathbb{R}^{d_e}$ be the vector of the natural coordinates of $\hat{P}$ and $\mathbf{x}_P = P - O = \left[x_1^P; \ldots; x_d^P\right] \in \mathbb{R}^d$
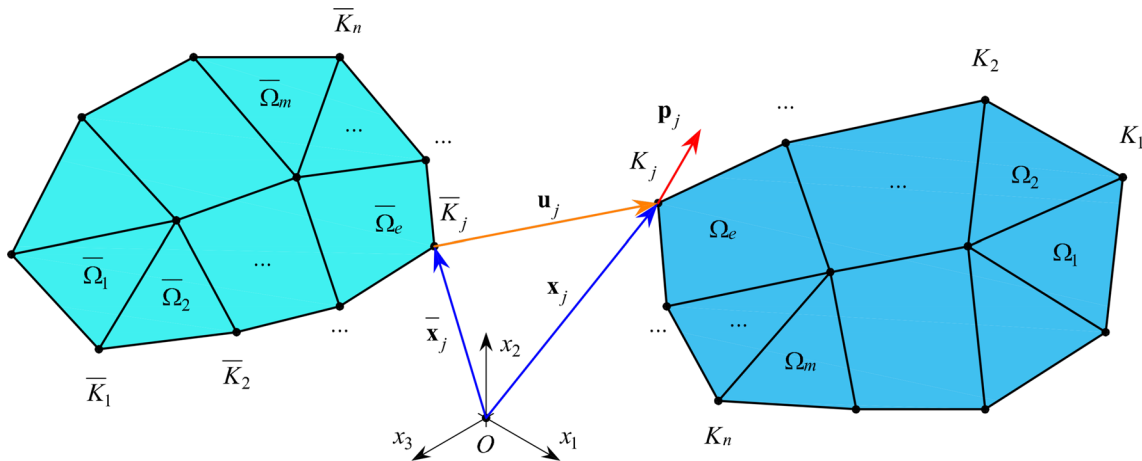
Fig. 1 Finite element discretisation: reference configuration (left) and current configuration (right). The Euclidean space dimension is $d = 3$

denote the position vector of P with respect to the global Cartesian reference system.

The mapping ϕ can be represented as follows:

$$\mathbf{x}_P = \mathbf{N}_e(\boldsymbol{\xi})\,\mathbf{x}_e, \tag{4}$$

where

$$\mathbf{N}_e(\boldsymbol{\xi}) = \left[N_1^e(\boldsymbol{\xi})\,\mathbf{I} \ldots N_{n_e}^e(\boldsymbol{\xi})\,\mathbf{I}\right] \in \mathbb{R}^{d \times n_e d} \tag{5}$$

is the shape function matrix of the element. Here, $N_k^e(\boldsymbol{\xi})$ (with $k = 1, \ldots, n_e$) are the nodal shape functions and $\mathbf{I} \in \mathbb{R}^{d \times d}$ is the identity matrix.

According to the isoparametric concept [1, 2], the reference configuration of the element, $\bar{\Omega}_e$, is obtained through a mapping, $\bar{\phi} : \hat{\Omega}_e \to \bar{\Omega}_e$, described by the same shape function matrix of Eq. (4). Thus, each point $\hat{P} \in \hat{\Omega}_e$ is mapped onto a point $\bar{P} = \bar{\phi}(\hat{P}) \in \bar{\Omega}_e$, whose position vector, $\bar{\mathbf{x}}_P = \bar{P} - O = [\bar{x}_1^P; \ldots; \bar{x}_d^P] \in \mathbb{R}^d$, is

$$\bar{\mathbf{x}}_P = \mathbf{N}_e(\boldsymbol{\xi})\,\bar{\mathbf{x}}_e, \tag{6}$$

where $\bar{\mathbf{x}}_e = \left[\bar{\mathbf{x}}_{j_1^e}; \ldots; \bar{\mathbf{x}}_{j_{n_e}^e}\right] \in \mathbb{R}^{n_e d}$ is the elemental nodal position vector in the reference configuration.

As a consequence of Eqs. (4) and (6), the displacement vector of point P turns out to be

$$\mathbf{u}_P = \mathbf{x}_P - \bar{\mathbf{x}}_P = \mathbf{N}_e(\boldsymbol{\xi})\,\mathbf{u}_e, \tag{7}$$

where $\mathbf{u}_e = \left[\mathbf{u}_{j_1^e}; \ldots; \mathbf{u}_{j_{n_e}^e}\right] = \mathbf{x}_e - \bar{\mathbf{x}}_e \in \mathbb{R}^{n_e d}$ is the nodal displacement vector of the element. Equation (7) shows that the displacement field of an isoparametric element is interpolated by the same shape functions used to describe its geometry.
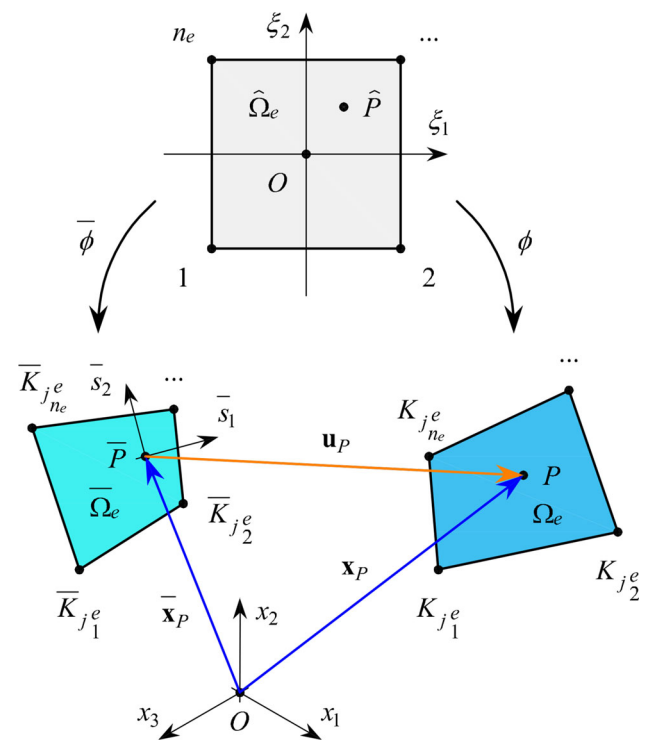

Fig. 2 Isoparametric mapping: parent element (top), mapped element in reference configuration (bottom, left), and mapped element in current configuration (bottom, right). The Euclidean space dimension is $d = 3$ and the element dimension is $d_e = 2$

2.3 Assembly

The nodal position and displacement vectors of an element can be expressed in terms of the corresponding global vectors as follows:

$$\mathbf{x}_e = \mathbf{A}_e\mathbf{x}, \quad \bar{\mathbf{x}}_e = \mathbf{A}_e\bar{\mathbf{x}}, \quad \text{and} \quad \mathbf{u}_e = \mathbf{A}_e\mathbf{u}, \tag{8}$$

where $\mathbf{A}_e \in \mathbb{R}^{n_e d \times nd}$ is the assembly matrix of the element [38].

For each element, $\mathbf{A}_e$ can be defined as a matrix having all null entries, except for the rows and columns corresponding to the element nodes. These are the rows from $(k-1)d+1$ to kd and columns from $(j_k^e - 1)d + 1$ to $j_k^e d$ (with $k = 1, \ldots, n_e$). In such positions, identity matrices, $\mathbf{I} \in \mathbb{R}^{d \times d}$, are placed.

The assembly matrices will be used in the following to formally describe the assembly procedure of the global stiffness matrices from the elemental matrices. However, direct implementation of Eq. (8) is not recommended because it may be computationally inefficient. Instead, the classical assembly procedure of the element stiffness matrices can be used [1].

2.4 Strain

At each point, $\bar{P}$, of the reference configuration, $\bar{\Omega}_e$, of an element, a local system of orthogonal coordinates, $\bar{s}_1, \ldots, \bar{s}_{d_e}$, is fixed. Let $\bar{\mathbf{a}}_1, \ldots, \bar{\mathbf{a}}_{d_e}$ be the unit vectors of the local axes. Then,

$$
\bar{\mathbf{Q}} = \begin{bmatrix} \mathbf{e}_1 \cdot \bar{\mathbf{a}}_1 \ldots \mathbf{e}_1 \cdot \bar{\mathbf{a}}_{d_e} \\ \vdots \qquad \vdots \\ \mathbf{e}_d \cdot \bar{\mathbf{a}}_1 \ldots \mathbf{e}_d \cdot \bar{\mathbf{a}}_{d_e} \end{bmatrix} \in \mathbb{R}^{d \times d_e} \tag{9}
$$

is the change-of-reference matrix that transforms the local coordinates into the global Cartesian coordinates. It is noted that, in general, the dimension of an element may be less than the dimension of the Euclidean space, so that $d_e < d$. In this case, $\bar{\mathbf{Q}}$ is a rectangular semi-orthogonal matrix. Instead, if the dimension of the element is equal to the space dimension, $d_e = d$, then $\bar{\mathbf{Q}}$ is a square orthogonal matrix.

The Green–Lagrange strain tensor, $\mathbf{E}$, is introduced as a suitable measure of finite deformations [39]. At each point $\bar{P} \in \bar{\Omega}_e$, the components of the strain tensor in the local coordinates can be expressed as

$$
E_{\alpha\beta} = \frac{1}{2} \left(\frac{\partial \mathbf{x}_P^{\mathsf{T}}}{\partial \bar{s}_\alpha} \frac{\partial \mathbf{x}_P}{\partial \bar{s}_\beta} - \frac{\partial \bar{\mathbf{x}}_P^{\mathsf{T}}}{\partial \bar{s}_\alpha} \frac{\partial \bar{\mathbf{x}}_P}{\partial \bar{s}_\beta} \right), \tag{10}
$$

where indices α and β range from 1 to d_e, and T denotes the transpose operation. By recalling Eqs. (4) and (6), the strain components can also be expressed as

$$
E_{\alpha\beta} = \frac{1}{2} \left(\mathbf{x}_e + \bar{\mathbf{x}}_e \right)^{\mathsf{T}} \Gamma_{\alpha\beta} \left(\mathbf{x}_e - \bar{\mathbf{x}}_e \right), \tag{11}
$$

where

$$
\Gamma_{\alpha\beta} = \frac{1}{2} \left(\frac{\partial \mathbf{N}_e^{\mathsf{T}}}{\partial \bar{s}_\alpha} \frac{\partial \mathbf{N}_e}{\partial \bar{s}_\beta} + \frac{\partial \mathbf{N}_e^{\mathsf{T}}}{\partial \bar{s}_\beta} \frac{\partial \mathbf{N}_e}{\partial \bar{s}_\alpha} \right) \in \mathbb{R}^{n_e d \times n_e d} \tag{12}
$$

make up a set of symmetric matrices. These Γ-matrices depend on the derivatives of the shape function matrix,

$$
\frac{\partial \mathbf{N}_e}{\partial \bar{s}_\alpha} = \left[\frac{\partial N_1^e}{\partial \bar{s}_\alpha} \mathbf{I} \ldots \frac{\partial N_{n_e}^e}{\partial \bar{s}_\alpha} \mathbf{I} \right], \tag{13}
$$

in turn depending on the derivatives of the single nodal shape functions. The latter can be evaluated through the chain rule as follows:

$$
\frac{\partial N_k^e}{\partial \bar{s}_\alpha} = \sum_{\gamma=1}^{d_e} \sum_{j=1}^{d} \frac{\partial N_k^e}{\partial \xi_\gamma} \frac{\partial \xi_\gamma}{\partial \bar{x}_j^P} \frac{\partial \bar{x}_j^P}{\partial \bar{s}_\alpha}. \tag{14}
$$

It is convenient to put Eq. (14) into matrix form. To this aim, let us first introduce the Jacobian matrix,

$$
\bar{\mathbf{J}} = \frac{\partial \bar{\mathbf{x}}_P}{\partial \boldsymbol{\xi}} = \left[\frac{\partial \mathbf{N}_e}{\partial \xi_1} \bar{\mathbf{x}}_e \ldots \frac{\partial \mathbf{N}_e}{\partial \xi_{d_e}} \bar{\mathbf{x}}_e \right] \in \mathbb{R}^{d \times d_e}, \tag{15}
$$

of the mapping $\bar{\phi} : \hat{\Omega}_e \to \bar{\Omega}_e$ described by Eq. (6) and the Jacobian matrix,

$$
\bar{\mathbf{J}}^+ = \frac{\partial \boldsymbol{\xi}}{\partial \bar{\mathbf{x}}_P} = \begin{bmatrix} \frac{\partial \xi_1}{\partial \bar{x}_1^P} \cdots \frac{\partial \xi_1}{\partial \bar{x}_d^P} \\ \vdots \qquad \vdots \\ \frac{\partial \xi_{d_e}}{\partial \bar{x}_1^P} \cdots \frac{\partial \xi_{d_e}}{\partial \bar{x}_d^P} \end{bmatrix} \in \mathbb{R}^{d_e \times d}, \tag{16}
$$

of the inverse mapping $\bar{\phi}^{-1} : \bar{\Omega}_e \to \hat{\Omega}_e$. Then, observing that

$$
\frac{\partial \bar{\mathbf{x}}_P}{\partial \bar{\mathbf{s}}} = \begin{bmatrix} \frac{\partial \bar{x}_1^P}{\partial \bar{s}_1} \cdots \frac{\partial \bar{x}_1^P}{\partial \bar{s}_{d_e}} \\ \vdots \qquad \vdots \\ \frac{\partial \bar{x}_d^P}{\partial \bar{s}_1} \cdots \frac{\partial \bar{x}_d^P}{\partial \bar{s}_{d_e}} \end{bmatrix} = \bar{\mathbf{Q}}, \tag{17}
$$

the following relationship in matrix form is obtained:

$$
\begin{bmatrix} \frac{\partial N_1^e}{\partial \bar{s}_1} \cdots \frac{\partial N_1^e}{\partial \bar{s}_{d_e}} \\ \vdots \qquad \vdots \\ \frac{\partial N_{n_e}^e}{\partial \bar{s}_1} \cdots \frac{\partial N_{n_e}^e}{\partial \bar{s}_{d_e}} \end{bmatrix} = \begin{bmatrix} \frac{\partial N_1^e}{\partial \xi_1} \cdots \frac{\partial N_1^e}{\partial \xi_{d_e}} \\ \vdots \qquad \vdots \\ \frac{\partial N_{n_e}^e}{\partial \xi_1} \cdots \frac{\partial N_{n_e}^e}{\partial \xi_{d_e}} \end{bmatrix} \bar{\mathbf{J}}^+ \bar{\mathbf{Q}}. \tag{18}
$$

It is worth noting that if $d_e = d$, then the Jacobian matrix of the inverse mapping is the inverse of the Jacobian matrix, $\bar{\mathbf{J}}^+ = \bar{\mathbf{J}}^{-1} \in \mathbb{R}^{d \times d}$. But, if $d_e < d$, then $\bar{\mathbf{J}}$ is a rectangular matrix, which has no standard inverse. In this case, the Moore-Penrose pseudo-inverse [40],

$$
\bar{\mathbf{J}}^+ = \left(\bar{\mathbf{J}}^{\mathsf{T}} \bar{\mathbf{J}} \right)^{-1} \bar{\mathbf{J}}^{\mathsf{T}}, \tag{19}
$$

can be used. Evidently, the pseudo-inverse of a square matrix coincides with the standard inverse.

Lastly, for what follows, it is useful to calculate the derivatives of the strain components from Eq. (11):

$$\frac{\partial E_{\alpha\beta}}{\partial \mathbf{x}_e} = \Gamma_{\alpha\beta}\mathbf{x}_e. \tag{20}$$

2.5 Stress

Stress will be represented through the second Piola–Kirchhoff stress tensor, $\mathbf{S}$, which is work-conjugate to the Green–Lagrange strain tensor, $\mathbf{E}$ [39].

Since the material is assumed to be hyperelastic, the stress tensor components can be derived from an elastic potential energy function, $\bar{\varphi}$, having the physical meaning of strain energy density:

$$S_{\alpha\beta} = \frac{\partial \bar{\varphi}}{\partial E_{\alpha\beta}}, \tag{21}$$

where α and β range from 1 to d_e.

2.6 Potential energy

In this work, the governing nonlinear static equilibrium equations are derived based on the principle of stationary total potential energy. To this aim, besides the assumption of hyperelastic material, the applied loads are assumed to be conservative. However, the latter hypothesis is not strictly required to deduce the expressions of the secant and tangent stiffness matrices.

The total potential energy of the system, $\mathcal{V}$, is the sum of the internal potential energy, $\mathcal{V}_{int}$, corresponding to the elastic strain energy, $\mathcal{U}$, and the external potential energy, $\mathcal{V}_{ext}$, which is the opposite of the virtual work of the applied loads, $\mathcal{W}$ [41]:

$$\mathcal{V} = \mathcal{V}_{int} + \mathcal{V}_{ext} = \mathcal{U} - \mathcal{W}. \tag{22}$$

The strain energy stored in the whole model can be computed by summing the contributions coming from each element:

$$\mathcal{U} = \sum_{e=1}^{m} \mathcal{U}_e, \tag{23}$$

where

$$\mathcal{U}_e = \int_{\bar{\Omega}_e} \bar{\varphi} \, \mathrm{d}\bar{V}_e \tag{24}$$

is the strain energy stored within the e-th element. In Eq. (24), the integration is carried out over the volume of the element, $\bar{V}_e$, in the reference configuration.

Besides, the virtual work done by the applied nodal loads on the corresponding displacements (from the reference configuration to the current configuration) is

$$\mathcal{W} = \sum_{j=1}^{n} \mathbf{p}_j^{\mathsf{T}} \mathbf{u}_j, \tag{25}$$

where $\mathbf{p}_j \in \mathbb{R}^d$ is the load vector applied to the j-th node. Here, it is assumed that all loads vary proportionally to a single load multiplier, λ. Hence, the global load vector, $\mathbf{p} = [\mathbf{p}_1; \ldots; \mathbf{p}_n] \in \mathbb{R}^{nd}$, can be expressed as

$$\mathbf{p} = \lambda\bar{\mathbf{p}}, \tag{26}$$

where $\bar{\mathbf{p}}$ is a reference load vector. As a consequence, the expression of the virtual work becomes

$$\mathcal{W} = \mathbf{p}^{\mathsf{T}}\mathbf{u} = \lambda\bar{\mathbf{p}}^{\mathsf{T}}(\mathbf{x} - \bar{\mathbf{x}}). \tag{27}$$

2.7 Equilibrium equations

Based on the previous assumptions, static equilibrium can be imposed through the stationarity of the total potential energy [41]. For the sake of simplicity, no kinematic restraints are here considered. If present, kinematic restraints can be included in the formulation of the problem as explained in Appendix B.

By recalling Eqs. (22) and (27), the nonlinear static equilibrium equations become:

$$\mathbf{g}(\mathbf{x}) = \frac{\partial \mathcal{V}}{\partial \mathbf{x}} = \frac{\partial \mathcal{U}}{\partial \mathbf{x}} - \frac{\partial \mathcal{W}}{\partial \mathbf{x}} = \mathbf{f}(\mathbf{x}) - \lambda\bar{\mathbf{p}} = \mathbf{0}, \tag{28}$$

where

$$\mathbf{f}(\mathbf{x}) = \frac{\partial \mathcal{U}}{\partial \mathbf{x}} \tag{29}$$

is the global elastic force vector.

2.8 Secant stiffness matrix

By recalling Eqs. (23) and (24), and applying the chain rule for differentiation, the elastic force vector can be expressed as

$$\mathbf{f}(\mathbf{x}) = \sum_{e=1}^{m} \int_{\bar{\Omega}_e} \sum_{\alpha=1}^{d_e} \sum_{\beta=1}^{d_e} \frac{\partial \bar{\varphi}}{\partial E_{\alpha\beta}} \frac{\partial E_{\alpha\beta}}{\partial \mathbf{x}} \, \mathrm{d}\bar{V}_e. \tag{30}$$

Furthermore, by recalling Eqs. (8), (20), and (21), the elastic force vector becomes

$$\mathbf{f}(\mathbf{x}) = \sum_{e=1}^{m} \mathbf{A}_e^{\mathsf{T}} \mathbf{f}_e(\mathbf{x}_e), \tag{31}$$

where

$$\mathbf{f}_e\left(\mathbf{x}_e\right) = \mathbf{S}_e\left(\mathbf{x}_e\right)\mathbf{x}_e \tag{32}$$

is the elastic force vector of the e-th element and

$$\mathbf{S}_e\left(\mathbf{x}_e\right) = \int_{\bar{\Omega}_e} \sum_{\alpha=1}^{d_e} \sum_{\beta=1}^{d_e} S_{\alpha\beta} \Gamma_{\alpha\beta} \, \mathrm{d}\bar{V}_e \tag{33}$$

is the secant stiffness matrix of the same element. Here, the matrix $\mathbf{S}_e\left(\mathbf{x}_e\right) \in \mathbb{R}^{n_e d \times n_e d}$ depends on the nodal position vector, $\mathbf{x}_e$, of the element and is always symmetric because of the symmetry of the Γ-matrices defined in Eq. (12).

In general, the evaluation of the integral in Eq. (33) may require numerical integration. This can be carried out by using the Gauss quadrature method [1, 2]:

$$\mathbf{S}_e\left(\mathbf{x}_e\right) \approx \sum_{h=1}^{g_e} \sum_{\alpha=1}^{d_e} \sum_{\beta=1}^{d_e} \left(S_{\alpha\beta} \Gamma_{\alpha\beta} \bar{J}\right)|_{\boldsymbol{\xi}=\boldsymbol{\xi}_h} w_h, \tag{34}$$

where $\bar{J} = 1/\det\left(\bar{\mathbf{J}}^+ \bar{\mathbf{Q}}\right)$, $\boldsymbol{\xi}_h$ is the vector of natural coordinates of the h-th Gauss point, w_h is the corresponding weight factor, and g_e is the number of Gauss points of the element.

From Eqs. (8), (31), and (32), the global elastic force vector,

$$\mathbf{f}\left(\mathbf{x}\right) = \mathbf{S}\left(\mathbf{x}\right)\mathbf{x}, \tag{35}$$

is determined as a function of the global secant stiffness matrix,

$$\mathbf{S}\left(\mathbf{x}\right) = \sum_{e=1}^{m} \mathbf{A}_e^{\mathsf{T}} \mathbf{S}_e\left(\mathbf{x}_e\right) \mathbf{A}_e. \tag{36}$$

Equation (36) symbolically represents the assembly procedure of the stiffness matrix [1]. It is worth noting that the global secant stiffness matrix, $\mathbf{S}\left(\mathbf{x}\right) \in \mathbb{R}^{nd \times nd}$, turns out to be always symmetric because of the symmetry of the assembled elemental matrices.

By substituting Eq. (35) into (28), the nonlinear static equilibrium equations take the form:

$$\mathbf{g}\left(\mathbf{x}\right) = \mathbf{S}\left(\mathbf{x}\right)\mathbf{x} - \lambda\bar{\mathbf{p}} = \mathbf{0}. \tag{37}$$

2.9 Tangent stiffness matrix

The implementation of incremental-iterative solution methods, as well as the evaluation of equilibrium stability, requires the introduction of the tangent stiffness matrix [2, 3]:

$$\mathbf{T}\left(\mathbf{x}\right) = \frac{\partial \mathbf{f}}{\partial \mathbf{x}} = \frac{\partial\left[\mathbf{S}\left(\mathbf{x}\right)\mathbf{x}\right]}{\partial \mathbf{x}}. \tag{38}$$

By recalling Eqs. (8), (20), (33), (35), and (36), the global tangent stiffness matrix can be expressed as follows:

$$\mathbf{T}\left(\mathbf{x}\right) = \sum_{e=1}^{m} \mathbf{A}_e^{\mathsf{T}} \mathbf{T}_e\left(\mathbf{x}_e\right) \mathbf{A}_e, \tag{39}$$

where

$$\mathbf{T}_e\left(\mathbf{x}_e\right) = \mathbf{S}_e\left(\mathbf{x}_e\right) +$$
$$+ \int_{\bar{\Omega}_e} \sum_{\alpha=1}^{d_e} \sum_{\beta=1}^{d_e} \sum_{\gamma=1}^{d_e} \sum_{\delta=1}^{d_e} C_{\alpha\beta\gamma\delta} \Gamma_{\alpha\beta} \mathbf{x}_e \mathbf{x}_e^{\mathsf{T}} \Gamma_{\gamma\delta} \, \mathrm{d}\bar{V}_e \tag{40}$$

is the tangent stiffness matrix of the e-th element. In Eq. (40),

$$C_{\alpha\beta\gamma\delta} = \frac{\partial S_{\alpha\beta}}{\partial E_{\gamma\delta}} = \frac{\partial^2 \bar{\varphi}}{\partial E_{\alpha\beta} \partial E_{\gamma\delta}}, \tag{41}$$

with $\alpha, \beta, \gamma, \delta = 1, \ldots, d_e$, are the components of the fourth-order material elasticity tensor [13].

From inspection of Eqs. (39) and (40), it is clear that both $\mathbf{T}\left(\mathbf{x}\right) \in \mathbb{R}^{nd \times nd}$ and $\mathbf{T}_e\left(\mathbf{x}_e\right) \in \mathbb{R}^{n_e d \times n_e d}$ are symmetric matrices. Also, it is worth noting that since $\mathbf{x}$ and $\mathbf{u}$ differ by a constant, the position-based tangent stiffness matrix, $\mathbf{T}\left(\mathbf{x}\right)$, is numerically coincident with the displacement-based tangent stiffness matrix, $\mathbf{K}_{\mathrm{T}}\left(\mathbf{u}\right)$. In particular, the two addends in Eq. (40) correspond to the so-called initial stress and constitutive contributions to the tangent stiffness matrix [13]. Interestingly, since $\mathbf{S}_e\left(\mathbf{x}_e\right)$ depends on the stress components, $S_{\alpha\beta}$, compressive (negative) stresses add negatively to the structural stiffness. This qualitatively explains why increasing compressive stresses may cause a progressive loss of structural stiffness, ultimately leading to local and global instability phenomena.

Similarly to Eq. (34), the integral in Eq. (40) may be evaluated numerically by using the Gauss quadrature method [1, 2]:

$$\mathbf{T}_e\left(\mathbf{x}_e\right) \approx \mathbf{S}_e\left(\mathbf{x}_e\right) +$$
$$+ \sum_{h=1}^{g_e} \sum_{\alpha=1}^{d_e} \sum_{\beta=1}^{d_e} \sum_{\gamma=1}^{d_e} \sum_{\delta=1}^{d_e} \left(C_{\alpha\beta\gamma\delta} \Gamma_{\alpha\beta} \mathbf{x}_e \mathbf{x}_e^{\mathsf{T}} \Gamma_{\gamma\delta} \bar{J}\right)|_{\boldsymbol{\xi}=\boldsymbol{\xi}_h} w_h. \tag{42}$$

3 Applications

3.1 Truss bar element

As a first application, a one-dimensional ($d_e = 1$), two-node ($n_e = 2$) truss bar element is developed, which can be used to model both planar ($d = 2$) and spatial ($d = 3$) structures.
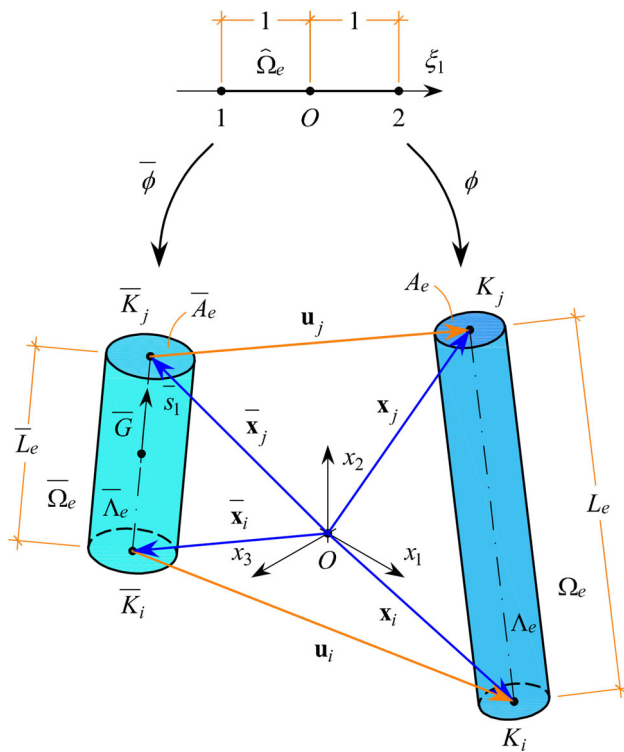
Fig. 3 Truss bar element: parent element (top), mapped element in reference configuration (bottom, left), and mapped element in current configuration (bottom, right)

In a general configuration, the element is supposed to occupy a region, Ω_e, in the shape of a right cylinder with straight centreline, Λ_e, and constant cross-section area, A_e. The two nodes of the element are placed at the centres of the cylinder bases. Let $i = j_1^e$ and $j = j_2^e$ denote the indices of the element nodes. Thus, $\mathbf{x}_i = K_i - O$ and $\mathbf{x}_j = K_j - O$ are the position vectors of the element nodes and $\mathbf{x}_e = [\mathbf{x}_i; \mathbf{x}_j] \in \mathbb{R}^{2d}$ is the nodal position vector of the element. The same quantities in the reference configuration will be distinguished by bars on top of the symbols (Fig. 3).

Let us define

$$\mathbf{L}_{ij} = \mathbf{x}_j - \mathbf{x}_i = [-\mathbf{I} \ \mathbf{I}]\, \mathbf{x}_e \tag{43}$$

as the vector going from K_i to K_j. Then, the squared length of the bar can be calculated as

$$L_e^2 = \|\mathbf{L}_{ij}\|^2 = \mathbf{L}_{ij}^\mathsf{T} \mathbf{L}_{ij}. \tag{44}$$

By substituting Eq. (43) into (44), the squared length can be also expressed as

$$L_e^2 = \mathbf{x}_e^\mathsf{T} \Delta \mathbf{x}_e, \tag{45}$$

where the following nodal-position difference matrix,

$$\Delta = \begin{bmatrix} \mathbf{I} & -\mathbf{I} \\ -\mathbf{I} & \mathbf{I} \end{bmatrix}, \tag{46}$$

has been introduced.

For the truss bar element, the only relevant strain and stress components are in the axial direction. To calculate such components, a local coordinate, $\bar{s}_1$, is fixed in the reference configuration of the element, $\bar{\Omega}_e$. The local $\bar{s}_1$-axis is placed with the origin at the midpoint, $\bar{G}$, of the bar centreline, $\bar{\Lambda}_e$, in the direction going from $\bar{K}_i$ towards $\bar{K}_j$. The corresponding unit vector is

$$\bar{\mathbf{a}}_1 = \frac{1}{\bar{L}_e} \bar{\mathbf{L}}_{ij}, \tag{47}$$

where $\bar{\mathbf{L}}_{ij} = \bar{\mathbf{x}}_j - \bar{\mathbf{x}}_i$ and $\bar{L}_e = \|\bar{\mathbf{L}}_{ij}\|$. The change-of-reference matrix, Eq. (9), turns out to be

$$\bar{\mathbf{Q}} = \bar{\mathbf{a}}_1 \in \mathbb{R}^{d \times 1}. \tag{48}$$

The parent element can be represented as $\hat{\Omega}_e = [-1, 1] \subset \mathbb{R}$. A single natural coordinate, ξ_1, is introduced and linear shape functions are assumed as follows:

$$\begin{aligned} N_1^e(\xi_1) &= \frac{1}{2}(1 - \xi_1), \\ N_2^e(\xi_1) &= \frac{1}{2}(1 + \xi_1). \end{aligned} \tag{49}$$

The shape function matrix, Eq. (5), is

$$\mathbf{N}_e(\xi_1) = \frac{1}{2}\left[(1 - \xi_1)\, \mathbf{I} \ (1 + \xi_1)\, \mathbf{I}\right] \tag{50}$$

By substituting Eq. (50) into (15), the Jacobian matrix can be calculated as

$$\bar{\mathbf{J}} = \frac{1}{2}(\bar{\mathbf{x}}_j - \bar{\mathbf{x}}_i) = \frac{1}{2}\bar{\mathbf{L}}_{ij} \in \mathbb{R}^{d \times 1} \tag{51}$$

and its pseudo-inverse, also recalling Eq. (44), turns out to be

$$\bar{\mathbf{J}}^+ = \frac{2}{\bar{L}_e^2} \bar{\mathbf{L}}_{ij}^\mathsf{T} \in \mathbb{R}^{1 \times d}. \tag{52}$$

By substituting Eqs. (47), (48), (49), and (52) into (18), and again recalling Eq. (44), the derivatives of the shape functions are obtained as

$$\frac{\partial N_1^e}{\partial \bar{s}_1} = -\frac{1}{\bar{L}_e} \quad \text{and} \quad \frac{\partial N_2^e}{\partial \bar{s}_1} = \frac{1}{\bar{L}_e}. \tag{53}$$

Hence,

$$\frac{\partial \mathbf{N}_e}{\partial \bar{s}_1} = \frac{1}{\bar{L}_e} \left[-\mathbf{I} \ \mathbf{I} \right]. \tag{54}$$

By substituting Eq. (54) into (12), the following Γ-matrix is obtained:

$$\Gamma_{11} = \left(\frac{\partial \mathbf{N}_e}{\partial \bar{s}_1} \right)^{\mathsf{T}} \frac{\partial \mathbf{N}_e}{\partial \bar{s}_1} = \frac{1}{\bar{L}_e^2} \Delta. \tag{55}$$

Next, by substituting Eq. (55) into (11), the axial component of the Green–Lagrange strain in the bar element,

$$E_{11} = \frac{1}{2\bar{L}_e^2} (\mathbf{x}_e + \bar{\mathbf{x}}_e)^{\mathsf{T}} \Delta (\mathbf{x}_e - \bar{\mathbf{x}}_e), \tag{56}$$

is determined.

Lastly, by substituting Eq. (55) into (33) and (40), and observing that the integrand functions are constant in the reference volume element, $\bar{V}_e = \bar{A}_e \bar{L}_e$, the secant stiffness matrix,

$$\mathbf{S}_e = S_{11} \frac{\bar{A}_e}{\bar{L}_e} \Delta, \tag{57}$$

and tangent stiffness matrix,

$$\mathbf{T}_e = S_{11} \frac{\bar{A}_e}{\bar{L}_e} \Delta + C_{1111} \frac{\bar{A}_e}{\bar{L}_e^3} \Delta \mathbf{x}_e \mathbf{x}_e^{\mathsf{T}} \Delta, \tag{58}$$

of the truss bar element are obtained. In Eq. (58),

$$C_{1111} = \frac{\partial S_{11}}{\partial E_{11}} = \frac{\partial^2 \bar{\varphi}}{\partial E_{11}^2} \tag{59}$$

is the component of the material elasticity tensor in the bar axial direction or, in other words, the tangent elastic modulus of the material.

More explicit expressions of Eqs. (57) and (58) can be obtained, once the constitutive relationship between the axial components of the second Piola–Kirchhoff stress, S_{11}, and Green–Lagrange strain, E_{11}, are specified. Examples of such relationships are given in Appendix C.2.

3.2 Plane triangular element

As a second application, a plane ($d_e = 2$) triangular element with three nodes ($n_e = 3$) is developed. The element can be used to model either plane stress or plane strain elasticity problems ($d = 2$), as well as planar ($d = 2$) or spatial ($d = 3$) thin membranes.

In a general configuration, the element is supposed to occupy a region, Ω_e, in the shape of a right triangular prism.
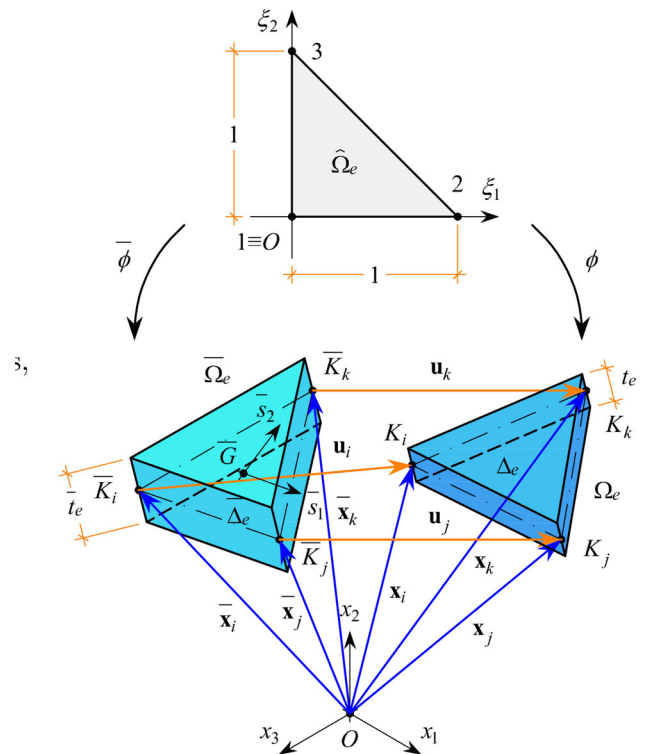

Fig. 4 Plane triangular element: parent element (top), mapped element in reference configuration (bottom, left), and mapped element in current configuration (bottom, right)

The height of the prism—corresponding to the thickness of the element—is denoted by t_e. The three nodes of the element are placed at the midpoints of the prism edges orthogonal to the triangular bases. Let $i = j_1^e$, $j = j_2^e$, and $k = j_3^e$ denote the indices of the element nodes. Thus, $\mathbf{x}_i = K_i - O$, $\mathbf{x}_j = K_j - O$, and $\mathbf{x}_k = K_k - O$ are the position vectors of the element nodes and $\mathbf{x}_e = \left[\mathbf{x}_i; \mathbf{x}_j; \mathbf{x}_k \right] \in \mathbb{R}^{3d}$ is the nodal position vector of the element. The same quantities in the reference configuration will be distinguished by bars on top of the symbols (Fig. 4).

For the formulation of the element, it is assumed that all quantities varying along the thickness can be reduced to the mid-plane triangle, Δ_e, defined by the positions of the three element nodes. Let us define

$$\mathbf{L}_{ij} = \mathbf{x}_j - \mathbf{x}_i = \left[-\mathbf{I} \ \mathbf{I} \ \mathbf{0} \right] \mathbf{x}_e \tag{60}$$

and

$$\mathbf{L}_{ki} = \mathbf{x}_i - \mathbf{x}_k = \left[\mathbf{I} \ \mathbf{0} \ -\mathbf{I} \right] \mathbf{x}_e \tag{61}$$

as the vectors going from K_i to K_j and from K_k to K_i, respectively. Then, the internal angle, α_i, of the triangle Δ_e at vertex K_i can be calculated from

$$\cos \alpha_i = -\frac{\mathbf{L}_{ij}^{\mathsf{T}} \mathbf{L}_{ki}}{L_{ij} L_{ki}}, \tag{62}$$

where $L_{ij} = \|\mathbf{L}_{ij}\|$ and $L_{ki} = \|\mathbf{L}_{ki}\|$. Besides, the area of Δ_e can be calculated as

$$A_e = \frac{1}{2} L_{ij} L_{ki} \sin \alpha_i. \tag{63}$$

For spatial problems ($d = 3$), the unit normal vector to the mid-plane of the element can be calculated through the following vector product:

$$\mathbf{n}_e = \frac{1}{2A_e} \mathbf{L}_{ki} \times \mathbf{L}_{ij}. \tag{64}$$

A system of local orthogonal coordinates is fixed in the reference configuration of the triangular element, $\bar{\Omega}_e$. Two local axes, $\bar{s}_1$ and $\bar{s}_2$, are placed in the mid-plane triangle, $\bar{\Delta}_e$, with origin at the centre point, $\bar{G}$, and directions respectively parallel and orthogonal to the direction going from $\bar{K}_i$ to $\bar{K}_j$. The unit vectors of the local axes can be expressed as

$$\bar{\mathbf{a}}_1 = \frac{1}{\bar{L}_{ij}} \bar{\mathbf{L}}_{ij}, \tag{65}$$

where $\bar{\mathbf{L}}_{ij} = \bar{\mathbf{x}}_j - \bar{\mathbf{x}}_i$ and $\bar{L}_{ij} = \|\bar{\mathbf{L}}_{ij}\|$, and

$$\bar{\mathbf{a}}_2 = \frac{\bar{L}_{ij}}{2\bar{A}_e} \left(\bar{\mathbf{a}}_1 \bar{\mathbf{a}}_1^{\mathsf{T}} - \mathbf{I} \right) \bar{\mathbf{L}}_{ki}, \tag{66}$$

where $\bar{\mathbf{L}}_{ki} = \bar{\mathbf{x}}_i - \bar{\mathbf{x}}_k$ and $\bar{L}_{ki} = \|\bar{\mathbf{L}}_{ki}\|$.

The change-of-reference matrix, Eq. (9), turns out to be

$$\bar{\mathbf{Q}} = \left[\bar{\mathbf{a}}_1 \ \bar{\mathbf{a}}_2 \right] \in \mathbb{R}^{d \times 2}. \tag{67}$$

The parent element can be represented as $\hat{\Omega}_e = \{(\xi_1, \xi_2) : \xi_1 \in [0, 1], \xi_2 \in [0, 1 - \xi_1]\} \subset \mathbb{R}^2$, where ξ_1 and ξ_2 are the natural coordinates. Linear shape functions are assumed as follows:

$$N_1^e (\xi_1, \xi_2) = 1 - \xi_1 - \xi_2,$$
$$N_2^e (\xi_1, \xi_2) = \xi_1, \text{ and } N_3^e (\xi_1, \xi_2) = \xi_2. \tag{68}$$

The shape function matrix, Eq. (5), becomes

$$\mathbf{N}_e (\xi_1, \xi_2) = \left[(1 - \xi_1 - \xi_2) \mathbf{I} \ \xi_1 \mathbf{I} \ \xi_2 \mathbf{I} \right] \tag{69}$$

By substituting Eq. (69) into (15), the Jacobian matrix,

$$\bar{\mathbf{J}} = \left[\bar{\mathbf{L}}_{ij} \ -\bar{\mathbf{L}}_{ki} \right] \in \mathbb{R}^{d \times 2}, \tag{70}$$

is calculated. Its pseudo-inverse, also recalling Eqs. (62), (63), (65), and (66), turns out to be

$$\bar{\mathbf{J}}^+ = \frac{1}{2\bar{A}_e} \begin{bmatrix} \bar{L}_{ki} (\bar{\mathbf{a}}_1 \sin \bar{\alpha}_i - \bar{\mathbf{a}}_2 \cos \bar{\alpha}_i)^{\mathsf{T}} \\ \bar{L}_{ij} \bar{\mathbf{a}}_2^{\mathsf{T}} \end{bmatrix} \in \mathbb{R}^{2 \times d}, \tag{71}$$

where $\bar{\alpha}_i$ is the internal angle of the mid-plane triangle $\bar{\Delta}_e$ at $\bar{K}_i$ in the reference configuration.

By substituting Eqs. (67), (68), and (71) into (18), and again recalling Eq. (63), the derivatives of the shape functions are obtained as

$$\frac{\partial N_1^e}{\partial \bar{s}_1} = -\frac{1}{\bar{L}_{ij}}, \quad \frac{\partial N_2^e}{\partial \bar{s}_1} = \frac{1}{\bar{L}_{ij}}, \quad \frac{\partial N_3^e}{\partial \bar{s}_1} = 0, \tag{72}$$

$$\frac{\partial N_1^e}{\partial \bar{s}_2} = \frac{\bar{L}_1^{jk}}{2\bar{A}_e}, \quad \frac{\partial N_2^e}{\partial \bar{s}_2} = \frac{\bar{L}_1^{ki}}{2\bar{A}_e}, \quad \frac{\partial N_3^e}{\partial \bar{s}_2} = \frac{\bar{L}_1^{ij}}{2\bar{A}_e}, \tag{73}$$

where

$$\bar{L}_1^{ij} = \bar{\mathbf{a}}_1^{\mathsf{T}} \bar{\mathbf{L}}_{ij} = \bar{L}_{ij}, \quad \bar{L}_1^{jk} = \bar{\mathbf{a}}_1^{\mathsf{T}} \bar{\mathbf{L}}_{jk}, \quad \bar{L}_1^{ki} = \bar{\mathbf{a}}_1^{\mathsf{T}} \bar{\mathbf{L}}_{ki}, \tag{74}$$

with $\bar{\mathbf{L}}_{jk} = \bar{\mathbf{x}}_k - \bar{\mathbf{x}}_j$.

By substituting Eqs. (72) and (73) into (12), the following Γ-matrices are obtained:

$$\Gamma_{11} = \frac{1}{\bar{L}_{ij}^2} \begin{bmatrix} \mathbf{I} & -\mathbf{I} & \mathbf{0} \\ -\mathbf{I} & \mathbf{I} & \mathbf{0} \\ \mathbf{0} & \mathbf{0} & \mathbf{0} \end{bmatrix}, \tag{75}$$

$$\Gamma_{12} = \frac{1}{4\bar{A}_e \bar{L}_{ij}} \begin{bmatrix} -2\bar{L}_1^{jk} \mathbf{I} & \left(\bar{L}_1^{jk} - \bar{L}_1^{ki} \right) \mathbf{I} & -\bar{L}_1^{ij} \mathbf{I} \\ \left(\bar{L}_1^{jk} - \bar{L}_1^{ki} \right) \mathbf{I} & 2\bar{L}_1^{ki} \mathbf{I} & \bar{L}_1^{ij} \mathbf{I} \\ -\bar{L}_1^{ij} \mathbf{I} & \bar{L}_1^{ij} \mathbf{I} & \mathbf{0} \end{bmatrix}, \tag{76}$$

and

$$\Gamma_{22} = \frac{1}{4\bar{A}_e^2} \begin{bmatrix} \left(\bar{L}_1^{jk} \right)^2 \mathbf{I} & \bar{L}_1^{jk} \bar{L}_1^{ki} \mathbf{I} & \bar{L}_1^{jk} \bar{L}_1^{ij} \mathbf{I} \\ \bar{L}_1^{ki} \bar{L}_1^{jk} \mathbf{I} & \left(\bar{L}_1^{ki} \right)^2 \mathbf{I} & \bar{L}_1^{ki} \bar{L}_1^{ij} \mathbf{I} \\ \bar{L}_1^{ij} \bar{L}_1^{jk} \mathbf{I} & \bar{L}_1^{ij} \bar{L}_1^{ki} \mathbf{I} & \left(\bar{L}_1^{ij} \right)^2 \mathbf{I} \end{bmatrix}. \tag{77}$$

Then, from Eqs. (33) and (40), by observing that the integrand functions are constant in the reference volume of the element, $\bar{V}_e = \bar{A}_e \bar{t}_e$, the secant stiffness matrix,

$$\mathbf{S}_e = (S_{11} \Gamma_{11} + 2S_{12} \Gamma_{12} + S_{22} \Gamma_{22}) \bar{V}_e, \tag{78}$$

and tangent stiffness matrix,

$$\mathbf{T}_e = \mathbf{S}_e + \sum_{\alpha=1}^{2} \sum_{\beta=1}^{2} \sum_{\gamma=1}^{2} \sum_{\delta=1}^{2} C_{\alpha\beta\gamma\delta} \Gamma_{\alpha\beta} \mathbf{x}_e \mathbf{x}_e^{\mathsf{T}} \Gamma_{\gamma\delta} \bar{V}_e, \tag{79}$$

of the triangular element are obtained. In Eq. (79),

$$C_{\alpha\beta\gamma\delta} = \frac{\partial S_{\alpha\beta}}{\partial E_{\gamma\delta}} = \frac{\partial^2 \bar{\varphi}}{\partial E_{\alpha\beta} \partial E_{\gamma\delta}}, \qquad (80)$$

with $\alpha, \beta, \gamma, \delta \in \{1, 2\}$, are the components of the material elasticity tensor in the local reference of the element.

4 Numerical examples

4.1 Constitutive laws

One of the main advantages of the present formulation is that any hyperelastic constitutive law can be implemented by simply introducing the suitable expressions of the stress and material elasticity tensor components into Eqs. (33) and (40), respectively.

For the sake of illustration, in the following examples, two material models are considered:

(i) a linear de Saint Venant–Kirchhoff material with strain energy density [13]:

$$\bar{\varphi} = \frac{1}{2}\lambda \left(I_1^E\right)^2 + \mu \, I_2^E, \qquad (81)$$

where $I_1^E = \operatorname{tr} \mathbf{E}$ and $I_2^E = \operatorname{tr} \mathbf{E}^2$ are the first and second invariants, respectively, of the Green–Lagrange strain tensor;

(ii) a neo-Hookean material with strain energy density [42]:

$$\bar{\varphi} = \frac{1}{4}\lambda \left(I_3^C - \ln I_3^C - 1\right) + \frac{1}{2}\mu \left(I_1^C - \ln I_3^C - 3\right), \qquad (82)$$

where $I_1^C = \operatorname{tr} \mathbf{C}$ and $I_3^C = \det \mathbf{C}$ are the first and third invariants, respectively, of the right Cauchy-Green strain tensor, $\mathbf{C} = 2\mathbf{E} + \mathbf{I}$.

In the above expressions, λ and μ are Lamé's parameters of the material, in turn related to the Young's modulus, E, and Poisson's ratio, ν, as follows:

$$\mu = \frac{E}{2\,(1 + \nu)},$$
$$\lambda = \frac{\nu E}{(1 + \nu)\,(1 - 2\nu)}. \qquad (83)$$

From Eqs. (81) and (82), the expressions of the components of the second Piola–Kirchhoff stress and material elasticity tensor can be derived by using Eqs. (21) and (41), respectively. In Appendix C, such expressions are worked out for the truss bar element in uniaxial stress and the plane triangular element in plane stress. The limiting case of
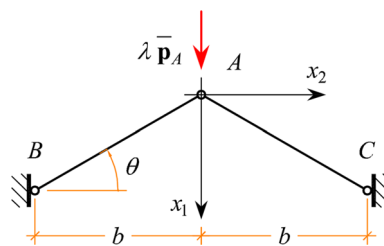

Fig. 5 Von Mises truss: a vertical load is applied to the crown node

incompressible material—corresponding to $\nu \to 1/2$, hence $\mu \to E/3$ and $\lambda \to +\infty$—is also explicitly calculated.

4.2 Von Mises truss

As a first example, the two-bar planar truss depicted in Fig. 5 is analysed using the element formulation of Sect. 3.1. This simple truss was originally proposed by von Mises [43, 44] as a prototype for the study of elastic instability phenomena.

Depending on the angle of inclination of bars, θ, von Mises trusses can be broadly classified as either 'shallow' or 'steep' (note that the exact distinction between the two cases depends on the assumed strain measure and constitutive law). The shallow von Mises truss is presented in textbooks as the typical structure featuring snap-through instability [41]. This type of response emerges even under the assumptions of small strains and linear constitutive law, provided that static equilibrium is imposed in the current configuration. However, Pecknold et al. [45] showed that, assuming finite strains and the SVK material model, steep von Mises trusses also feature bifurcation instability. They obtained the analytical solution for a symmetric two-bar truss subject to vertical and horizontal loading. Ligarò and Valvo [46] extended such solution to asymmetric two-bar trusses. Pelliciari and Tarantino [47] formulated the equilibrium problem for a symmetric von Mises truss under the general hypothesis of hyperelastic material. They deduced the analytical solution for Mooney-Rivlin material and showed a numerical example, where the equilibrium path is made of three separate branches. Fonseca and Gonçalves [48] investigated further the same problem, unveiling that for very steep two-bar trusses, the three separate branches of the equilibrium path merge and secondary bifurcation points arise. The interested reader can find further details and a more comprehensive literature survey in the recent papers by Pelliciari et al. [49] and Dao and Thi [50] (the latter with focus on dynamic analysis).

In the present study, a steep von Mises truss is considered. The following numerical values are taken from the work by Fonseca and Gonçalves [48]: half-base length, $b = 25$ mm; angle of inclination of bars, $\theta = 75$ deg; Lamé's material parameter, $\mu = 1.30$ MPa; Poisson's ratio, $\nu = 0.2$ and 0.5 for the compressible and incompressible cases, respectively.
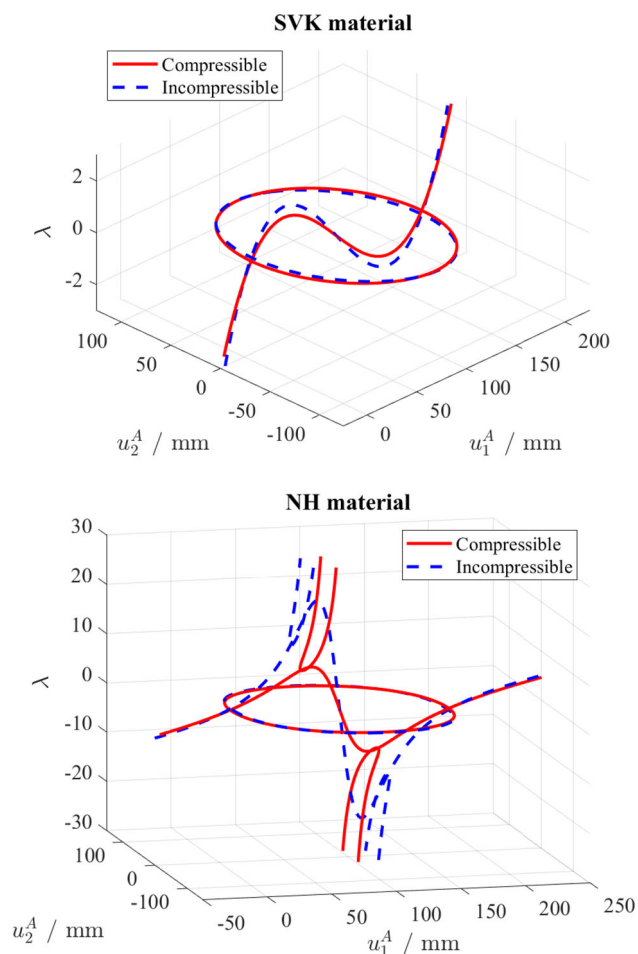
SVK material

NH material

Fig. 6 Equilibrium path of a steep von Mises truss subject to vertical loading according to the SVK (top) and NH (bottom) material models

The same material parameters are here used for both the SVK and NH material models. The reference load magnitude is $\|\bar{\mathbf{p}}_A\| = \mu \bar{A}_e/2$, where $\bar{A}_e$ is the bar cross-section area in the reference configuration.

A nonlinear analysis was conducted to trace the equilibrium path of the structure by using the admissible direction

cone (ADC) method by Ligarò and Valvo [46]. The ADC method improves the accuracy of the classical arc-length methods by Riks [51] and Crisfield [52] by varying the arc-length increment as a function of the local curvature of the path.

Figure 6 shows a three-dimensional view of the obtained equilibrium paths in the space of the load multiplier, λ, vs. the vertical and horizontal components of displacement, $\mathbf{u}_A$, of the crown node. According to the SVK material model, the path turns out to be composed of an S-shaped primary branch and an elliptic secondary branch. The primary branch exhibits two bifurcation points, at which it intersects the secondary branch, and two limit points. According to the NH material model, two more bifurcation points appear on the primary branch, from which two unbounded tertiary branches stem.

Table 1 reports the values obtained of the load multiplier at the first critical points on the primary branch. An excellent agreement can be appreciated between the results of present analysis and previous studies of the literature.

4.3 Cook's membrane

As a second example, the trapezoidal membrane depicted in Fig. 7 is analysed. The membrane is clamped on its major base and subject to a uniformly distributed shearing load, p_0, on its minor base. This problem was originally proposed by Cook [53, 54] to test the performances of some newly formulated quadrilateral finite elements in linear static analysis. More recently, Schröder et al. [42] selected Cook's membrane as a benchmark problem for nonlinear finite element analysis. They considered both plane strain and plane stress conditions, 2D and 3D finite element formulations, compressible and nearly incompressible materials, as well as elastic and elasto-plastic material models.

In the present study, Cook's membrane is analysed by using the 2D triangular element of Sect. 3.2 in plane stress conditions. Both structured and unstructured meshes were

Table 1 Results for the von Mises truss: load multiplier, λ, at critical points

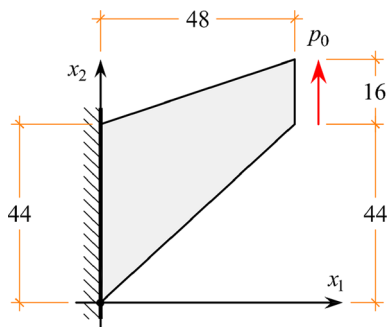| Material model	Behaviour	Critical point	λ (present)	λ [Ref.]
SVK	Incompressible	Bifurcation	0.7186	0.7186[45]
		Limit	2.0813	2.0813[45]
SVK	Compressible	Bifurcation	0.5748	0.5748[45]
		Limit	1.6650	1.6650[45]
NH	Incompressible	Bifurcation	1.1146	1.1[48]
		Bifurcation	13.3100	13.3[48]
		Limit	22.2600	22.3[48]
NH	Compressible	Bifurcation	0.8189	–
		Bifurcation	8.2480	–
		Limit	8.8193	–

Fig. 7 Cook's membrane. The major base is clamped to a fixed support. A uniformly distributed shearing load is applied on the free vertical edge. All dimensions are in mm. The thickness (not shown) is $t = 1$ mm
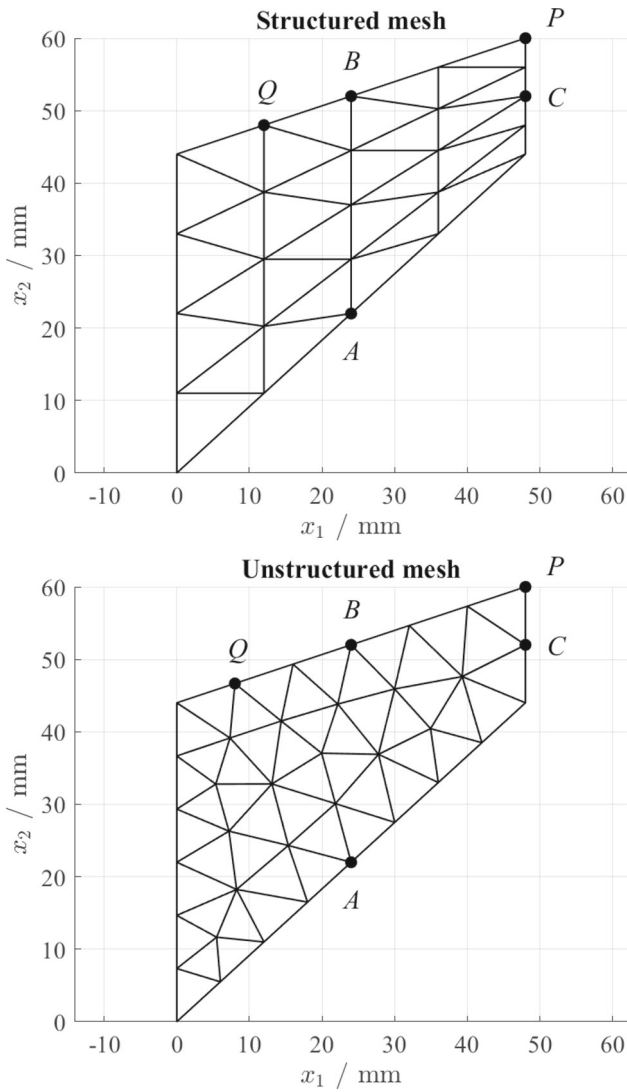
Table 2 Number of DOFs of structured and unstructured meshes of Cook's membrane

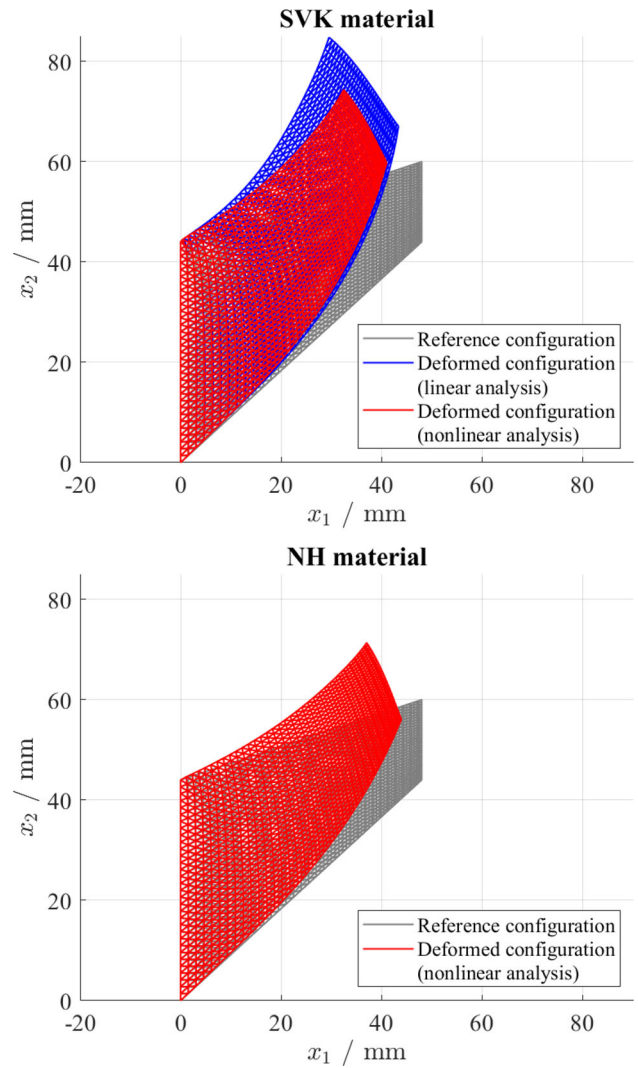| N_{subdiv}	Structured mesh N	Unstructured mesh N
2	18	74
4	50	248
8	162	912
16	578	3,496
32	2,178	13,578
64	8,450	53,686

Fig. 9 Analysis of Cook's membrane with the SVK (top) and NH (bottom) material models: reference and deformed configurations. The figure refers to a structured mesh with $N = 2, 178$ DOFs ($N_{subdiv} = 32$)

Fig. 8 Finite element model of Cook's membrane: structured mesh with $N_{subdiv} = 4$ (top) and unstructured mesh with $N_{subdiv} = 2$ (bottom). Reference nodes for checking the analysis results are: A, midpoint of lower edge; B, midpoint of upper edge; C, midpoint of minor base; P, top right corner; Q, leftmost free node on upper edge
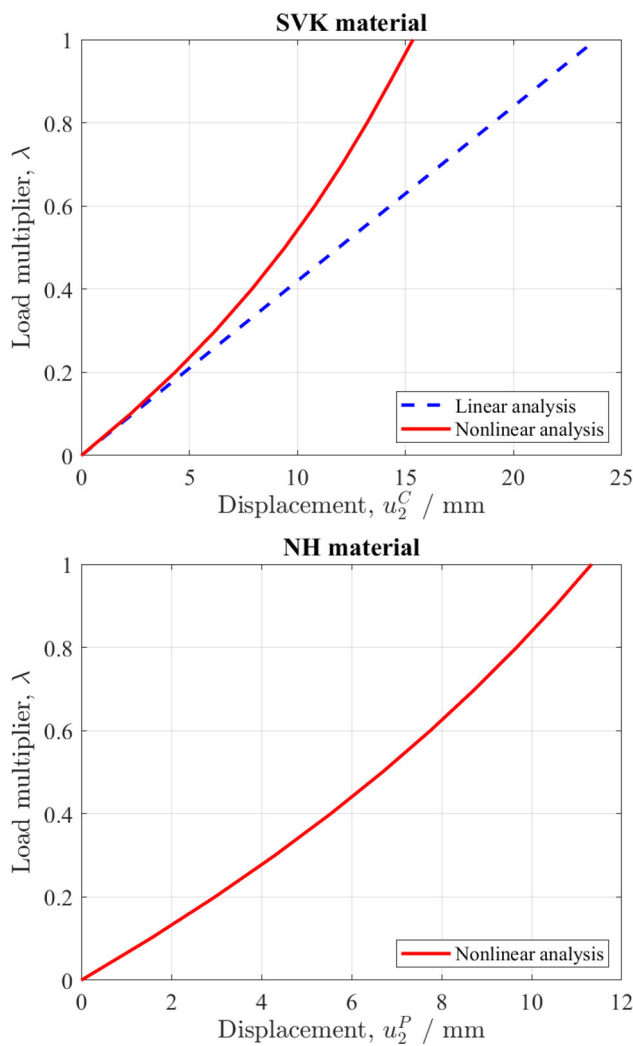
Fig. 10 Analysis of Cook's membrane with the SVK (top) and NH (bottom) material models: load multiplier vs. vertical displacement of reference nodes. The figure refers to a structured mesh with $N = 2{,}178$ DOFs ($N_{\mathrm{subdiv}} = 32$)

adopted (Fig. 8). The latter were created by using the *generateMesh* function available in the Partial Differential Equation Toolbox of MATLAB [55]. Convergence studies were conducted by checking the analysis results in terms of displacement and stress components at selected reference nodes. To this aim, more and more refined meshes were generated by progressively increasing the number of subdivisions, N_{subdiv}, of the minor base of the trapezoidal membrane. Table 2 shows the number, N, of DOFs of the structured and unstructured meshes. For the same number of subdivisions, unstructured meshes have a greater number of DOFs. Besides, unstructured meshes feature more uniform size and lower aspect ratio of elements—which is expected to improve convergence of the analyses.

Both the SVK and NH material models are considered. For the SVK model, the following numerical values are assumed from Cook's [54] paper: Young's modulus $E =$
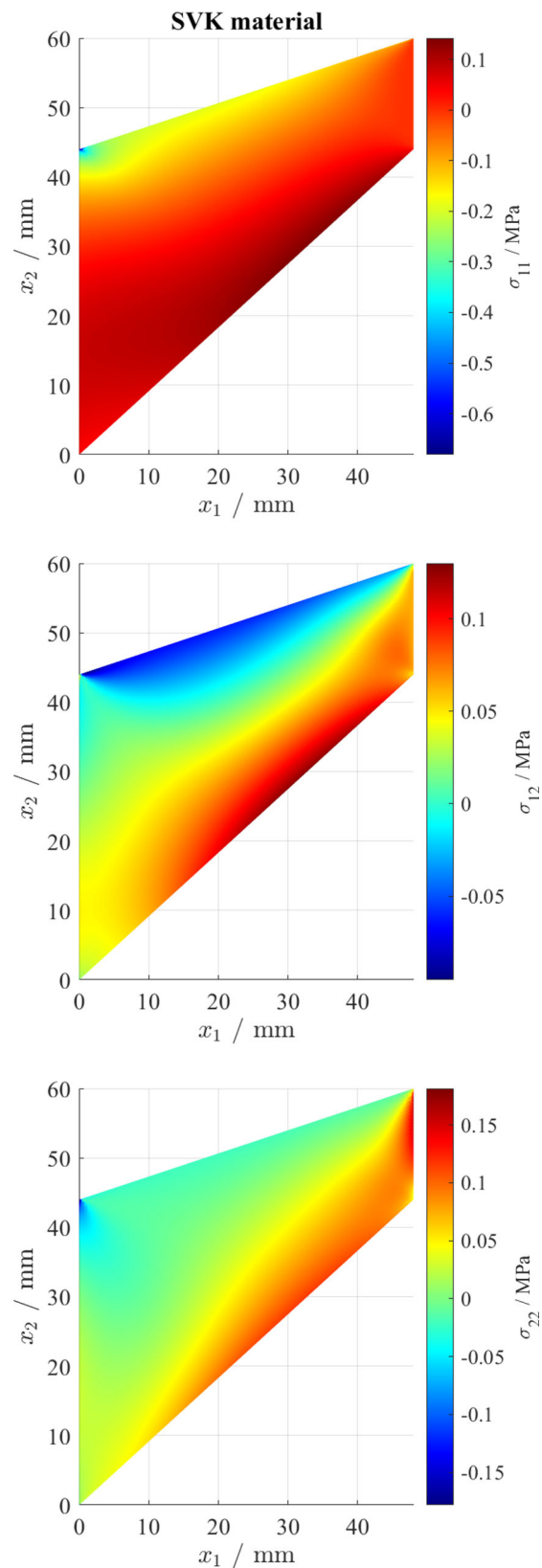

Fig. 11 Linear analysis of Cook's membrane with the SVK material: Cauchy stresses. The figure refers to an unstructured mesh with $N = 13{,}578$ DOFs ($N_{\mathrm{subdiv}} = 32$)
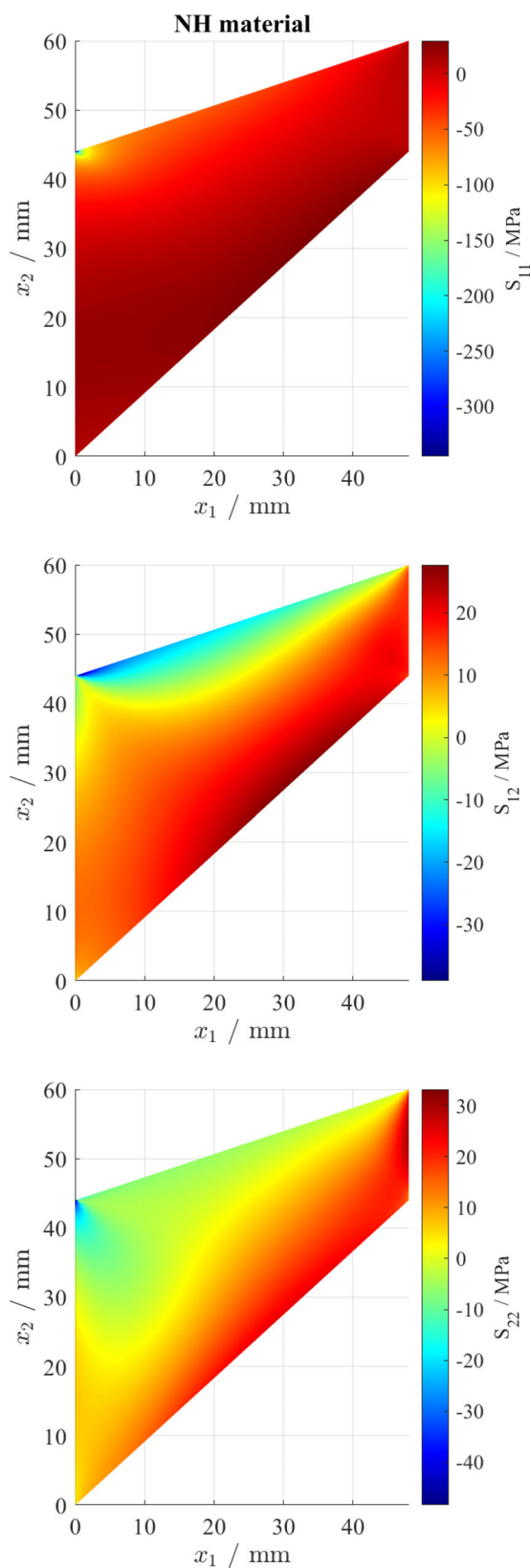
Fig. 12 Nonlinear analysis of Cook's membrane with the NH material: second Piola–Kirchhoff stresses. The figure refers to an unstructured mesh with $N = 13$, 578 DOFs ($N_{\mathrm{subdiv}} = 32$)

1 MPa; Poisson's ratio, $\nu = 1/3$; distributed shear load, $p_0 = 1 \, \mathrm{N}/(16 \times 1 \, \mathrm{mm}^2)$. For the NH model, the material properties are taken from the study by Schröder et al. [42]: Young's modulus $E = 500$ MPa; Poisson's ratio, $\nu = 0.35$; distributed shear load, $p_0 = 20 \, \mathrm{N/mm}^2$.

For the SVK material model, first, a linear analysis was conducted to compare the present results with those by Cook [54]. To this aim, the tangent stiffness matrix of the model was evaluated in the reference configuration and inverted to calculate the displacements produced by the assigned loads. Then, a geometrically nonlinear analysis was conducted under load control. The assigned load was applied step by step by increasing the load multiplier, λ, between 0 and 1. At each incremental step, Newton–Raphson's iterative method was used to achieve convergence. For the NH material model, only the nonlinear analysis under load control was conducted.

Typical analysis results are shown in Figs. 9, 10, 11, and 12. In particular, Fig. 9 depicts some exemplary reference and deformed configurations: it can be noted that the linear analysis predicts larger displacements with respect to the nonlinear analysis. This is confirmed by the load vs. displacement plots in Fig. 10: nonlinear analysis highlights a stiffening response with the increase of load level. Figures 11 and 12 show typical stress contour plots obtained from linear and nonlinear analyses, respectively. These plots were created by using the *griddata* function available in MATLAB [55] to interpolate and extrapolate the stress values calculated at the centroids of the elements over the whole region occupied by the membrane.

Tables 3, 4, and 5 summarise the results of the convergence study conducted for the linear analysis with the SVK material. The vertical displacement, u_2^C, of node C, the maximum principal stress, σ_{I}^A, at node A, and the minimum principal stress, σ_{II}^B, at node B are reported as functions of the number, N, of DOFs. The principal stresses were calculated from the node-averaged global stress components evaluated at the centroids of the adjacent elements. The same results are also shown in graphical form in Fig. 13. As the number of DOFs increases, all the considered results converge for both structured and unstructured meshes: as expected, unstructured meshes perform better and achieve convergence faster than structured meshes. A good agreement is observed with the same quantities calculated by Cook [54] with hybrid local (HL) and hybrid global (HG) quadrilateral elements. Cook's analyses reached convergence with fewer elements: in this respect, it should be noted that he used quadrilateral elements with variable strain and stress, while the present study adopts triangular elements with constant strain and stress.

Table 6 shows the results of the convergence study conducted for the geometrically nonlinear analysis with the SVK material. It is noteworthy that, contrary to linear analysis, the vertical displacement of the reference node, u_2^C, does

Table 3 Linear analysis of Cook's membrane with the SVK material: convergence study for the vertical displacement of node C

Structured mesh		Unstructured mesh		HL elements [54]		HG elements [54]	
N	u_2^C/mm	N	u_2^C/mm	N	u_2^C/mm	N	u_2^C/mm
18	11.9928	74	21.0768	18	18.169	18	22.323
50	18.2837	248	23.1536	50	22.023	50	23.516
162	22.0224	912	23.7436	162	23.393	162	23.803
578	23.4120	3,496	23.9039	578	23.805	578	23.911
2,178	23.8155	13,578	23.9483	–	–	–	–
8,450	23.9241	53,686	23.9617	–	–	–	–

Table 4 Linear analysis of Cook's membrane with the SVK material: convergence study for the maximum principal stress at node A

Structured mesh		Unstructured mesh		HL elements [54]		HG elements [54]	
N	σ_{I}^A/MPa	N	σ_{I}^A/MPa	N	σ_{I}^A/MPa	N	σ_{I}^A/MPa
18	0.0760	74	0.1763	18	0.1582	18	0.0933
50	0.1498	248	0.2112	50	0.1980	50	0.1628
162	0.1999	912	0.2277	162	0.2205	162	0.2060
578	0.2217	3,496	0.2327	578	0.2294	578	0.2225
2,178	0.2303	13,578	0.2343	–	–	–	–
8,450	0.2339	53,686	0.2356	–	–	–	–

Table 5 Linear analysis of Cook's membrane with the SVK material: convergence study for the minimum principal stress at node B

Structured mesh		Unstructured mesh		HL elements [54]		HG elements [54]	
N	σ_{II}^B/MPa	N	σ_{II}^B/MPa	N	σ_{II}^B/MPa	N	σ_{II}^B/MPa
18	−0.0360	74	−0.1262	18	−0.1335	18	−0.1394
50	−0.1002	248	−0.1687	50	−0.1700	50	−0.1566
162	−0.1567	912	−0.1908	162	−0.1931	162	−0.1844
578	−0.1844	3,496	−0.1978	578	−0.2005	578	−0.1952
2,178	−0.1954	13,578	−0.2001	–	–	–	–
8,450	−0.1999	53,686	−0.2020	–	–	–	–

not converge with mesh refinement. Indeed, for the meshes with larger number of DOFs, the analyses under load control failed before reaching the assigned load level ($\lambda = 1$). In such cases, application of the ADC arc-length method [46] showed that a limit point with $\lambda < 1$ is present in the equilibrium paths (Fig. 14). As a matter of fact, as the meshes get finer, larger compressive stresses develop in the neighbourhood of the upper left corner of the membrane (where a theoretical stress singularity is expected). Such large compressive stresses—associated to the higher deformability of the finer meshes and the softening behaviour of the SVK material in compression—lead to local instability. Similar instability issues have been reported, amongst others, by Düster et al. [56] and Pascon [57].

Moving on to the nonlinear analysis with the NH material, Tables 7, 8, and 9 show the results of the convergence study in terms of the vertical displacement of the reference node, P, and the maximum and minimum principal stresses, S_{I}^A and S_{II}^B, at nodes A and B, respectively. The same results are also shown in Fig. 15 in graphical form. As the number, N,

of DOFs increases, all the considered quantities converge for both structured and unstructured meshes. An excellent agreement can be observed with the results obtained by Schröder et al. [42] with hexaedral p-FEM and tetrahedral mixed displacement-pressure ($T_2 P_0$) elements. It should be noted, however, that the p-FEM elements enable faster convergence thanks to their higher-order shape functions.

Lastly, the behaviour is evaluated of the formulated triangular element for nearly incompressible and incompressible materials. Following Schröder et al. [42], one of Lamé's material parameters, $\mu = 500/2.7$ MPa ≈ 185.185 MPa, is kept fixed, while the other one, λ, is suitably increased, so that Poisson's ratio approaches the incompressibility limit. For this study, the unstructured mesh with $N = 53,686$ DOFs was used. Results of this parametric study are presented in Table 10. A very good agreement can be appreciated with the results obtained by Schröder et al. [42] for nearly incompressible materials. The present formulation was able to deal also with the perfectly incompressible case ($\nu = 0.5$), which was not calculated in the cited study.
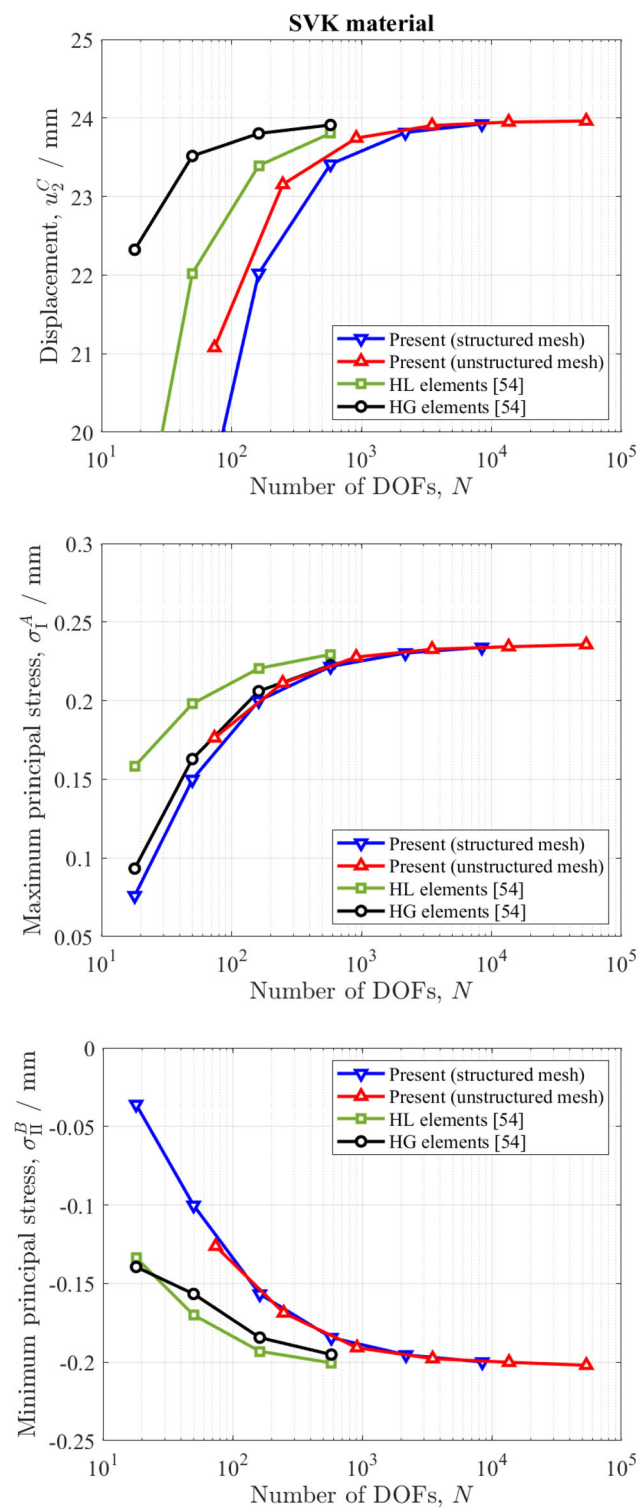
SVK material

Fig. 13 Linear analysis of Cook's membrane with the SVK material: convergence study for the vertical displacement of node C (top), the maximum principal stress at node A (middle), and the minimum principal stress at node B (bottom)

Table 6 Geometrically nonlinear analysis of Cook's membrane with the SVK material: convergence study for the vertical displacement of node C

Structured mesh		Unstructured mesh	
N	u_2^C/mm	N	u_2^C/mm
18	10.3524	74	14.4406
50	13.4883	248	15.0839
162	14.7593	912	15.2823
578	15.1620	3,496	*
2,178	15.3439	13,578	*
8,450	*	53,686	*

* No solution for $\lambda = 1$ due to a limit point with $\lambda < 1$

5 Discussion

The main advantage of the proposed position-based formulation lies in the simplicity of its analytical formulation. The expressions of the secant and tangent stiffness matrices obtained in Sect. 2 for a general isoparametric element can be specialised for elements with any given dimension, d, and number of nodes, n_e. In Sect. 3, this procedure has been illustrated for a two-node truss bar element and a three-node triangular element.

Furthermore, any hyperelastic constitutive law can be easily implemented without having to rewrite the software code from scratch. This potential has been illustrated in Sect. 4 for the de Saint Venant–Kirchhoff and neo-Hookean material models. The present formulation is capable of dealing also with incompressible materials, as illustrated for truss bars and plane stress triangular elements. It should be mentioned, however, that for incompressible materials in plane strain, the PFEF—as well as the DFEF—might not work because the constitutive laws for the stress components become indeterminate. To overcome such difficulties, a mixed formulation with pressure DOFs could be adopted [58].

Contrary to most formulations of the literature, the secant stiffness matrices obtained from the present formulation turn out to be symmetric. This is favourable from the computational point of view as only the upper (or lower) triangular parts need to be computed and stored in the computer memory. Moreover, specialised algorithms can be used for their processing [59].

Compared to the standard DFEF, the PFEF is also advantageous in terms of computation time. For the sake of illustration, the analyses of the von Mises truss and Cook's membrane with the SVK material have been conducted also by using the DFEF according to Appendix A. For the von Mises truss, Table 11 shows the computation times, t_{DFEF} and t_{PFEF}, corresponding to the two formulations and their difference, $\Delta t = t_{\text{PFEF}} - t_{\text{DFEF}}$. The PFEF enabled a saving in computation time up to 8.6%. However, since the absolute
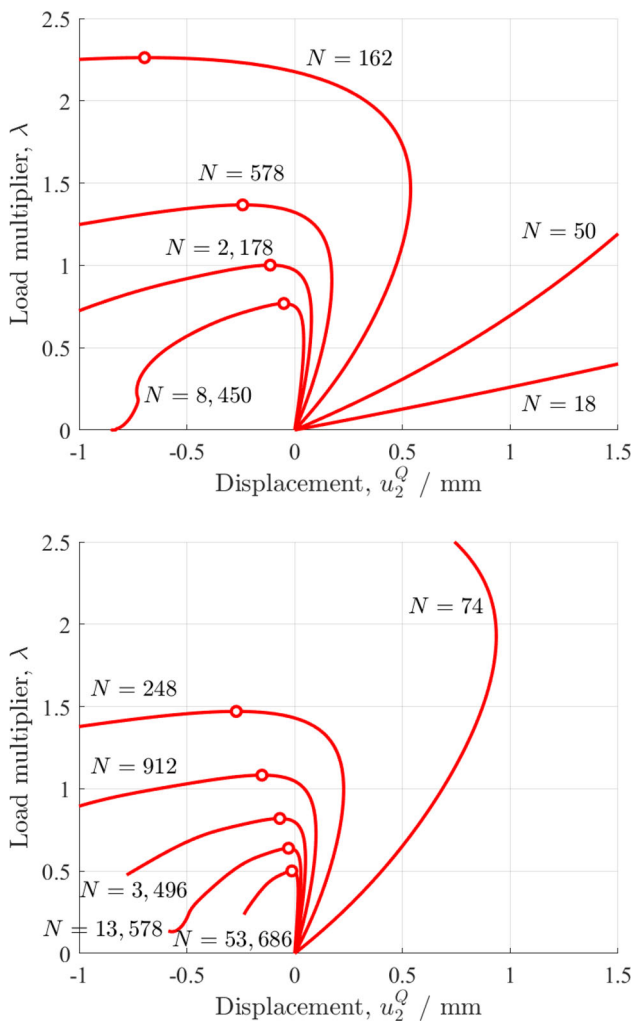
Fig. 14 Geometrically nonlinear analysis of Cook's membrane with the SVK material: view of the equilibrium paths in the plane of the vertical displacement of node Q (close to the upper left corner of the membrane) and load multiplier. The figure refers to structured (top) and unstructured (bottom) meshes with increasing number of DOFs, N. Circles mark the limit points for the load

Table 8 Nonlinear analysis of Cook's membrane with the NH material: convergence study for the maximum principal stress at node A

Structured mesh		Unstructured mesh	
N	S_{I}^{A}/MPa	N	S_{I}^{A}/MPa
18	21.7036	74	42.0551
50	37.0794	248	48.0001
162	45.9609	912	50.7050
578	49.6442	3,496	51.5268
2,178	51.0995	13,578	51.8098
8,450	51.7072	53,686	52.0243

Table 9 Nonlinear analysis of Cook's membrane with the NH material: convergence study for the minimum principal stress at node B

Structured mesh		Unstructured mesh	
N	S_{II}^{B}/MPa	N	S_{II}^{B}/MPa
18	-9.3830	74	-31.0611
50	-24.5651	248	-40.3421
162	-37.9910	912	-47.1463
578	-45.0174	3,496	-48.9402
2,178	-48.0516	13,578	-49.3410
8,450	-49.3586	53,686	-50.0329

up to about 20%. This estimate is deemed to be more reliable, given the longer absolute computation times measured in this case.

6 Conclusions

A position-based finite element formulation has been introduced for the analysis of nonlinear elasticity problems. Simple analytical expressions have been deduced for the secant and tangent stiffness matrices of general isoparametric finite elements. Such expressions have been specialised for a two-node truss bar element and a three-node triangular element. Contrary to most formulations of the literature, the secant stiffness matrices turn out to be symmetric—with positive consequences from the computational point of view.
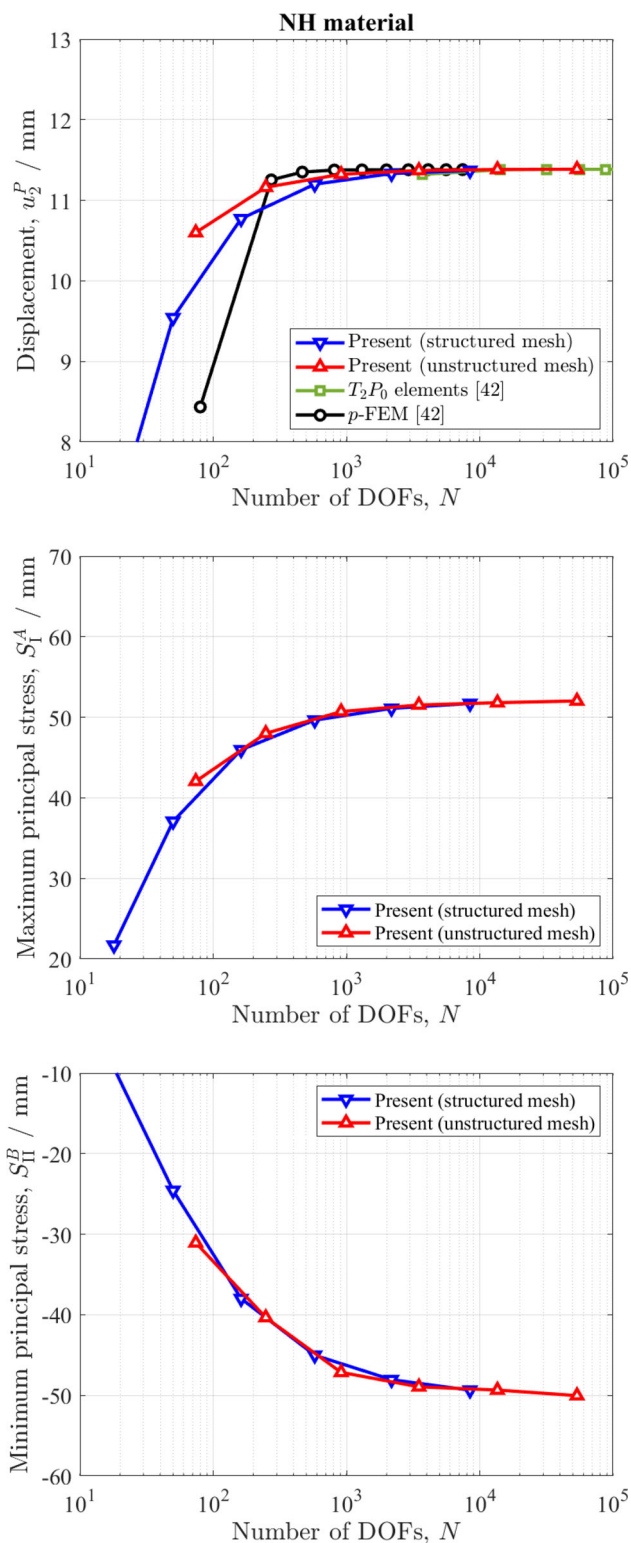
computation times are few tenths of a second, these results should be considered only as a general indication of the better performances of the PFEF. For Cook's membrane, Table 12 shows that the PFEF enabled savings in computation time

Table 7 Nonlinear analysis of Cook's membrane with the NH material: convergence study for the vertical displacement of node P

Structured mesh		Unstructured mesh		p-FEM [42]		$T_2 P_0$ elements [42]	
N	u_2^{P}/mm	N	u_2^{P}/mm	N	u_2^{P}/mm	N	u_2^{P}/mm
18	7.0138	74	10.5999	1,308	11.3781	3,696	11.3209
50	9.5423	248	11.1615	1,996	11.3782	14,304	11.3792
162	10.7716	912	11.3233	2,914	11.3793	31,824	11.3842
578	11.1999	3,496	11.3701	4,101	11.3803	56,256	11.3846
2,178	11.3318	13,578	11.3826	5,596	11.3808	87,600	11.3843
8,450	11.3708	53,686	11.3857	7,438	11.3811	125,856	11.3839

Fig. 15 Nonlinear analysis of Cook's membrane with the NH material: convergence study for the vertical displacement of node P (top), the maximum principal stress at node A (middle), and the minimum principal stress at node B (bottom)

Table 10 Nonlinear analysis of Cook's membrane with the NH material: parametric study for nearly incompressible materials

λ/MPa	ν	u_2^P/mm	u_2^P/mm [42]
432.1	0.35000	11.3857	11.3811
750	0.40099	11.1631	11.1564
9,260	0.49020	10.7930	10.7827
92,600	0.49900	10.7577	10.7464
926,000	0.49990	10.7541	10.7406
$+\infty$	0.50000	10.7537	–

Table 11 Analysis of the von Mises truss with the SVK material: comparison of computation times

Material behaviour	t_{DFEF}/s	t_{PFEF}/s	$\Delta t/t_{DFEF}$ (%)
Incompressible	0.308	0.282	-8.6
Compressible	0.287	0.279	-2.8

Table 12 Analysis of Cook's membrane with the SVK material: comparison of computation times

N	t_{DFEF}/s	t_{PFEF}/s	$\Delta t/t_{DFEF}$ (%)
18	0.069	0.057	-17.4
50	0.244	0.215	-11.9
162	0.856	0.653	-23.8
578	3.927	3.057	-22.2
2,178	18.229	14.194	-22.1

The formulation is valid for any hyperelastic constitutive law. In this paper, the de Saint Venant–Kirchhoff and neo-Hookean material models have been considered for illustration. The effectiveness of the proposed formulation has been proven through the analysis of two well-known benchmark problems: the von Mises truss and Cook's membrane. An excellent agreement has been found with previous results of the literature. Strengths and weaknesses of the proposed formulation have been discussed. In particular, the position-based formulation has been shown to be more computationally efficient than the standard displacement-based formulation.

Possible future developments of the present research include, but are not limited to:

– implementation of other hyperelastic material models, for instance to analyse wrinkling [60] and anisotropic membranes [61];
– formulation of three-dimensional and higher-order elements: this development only requires the specialisation of the general expressions of the stiffness matrices here deduced for isoparametric elements;

– formulation of structural elements for the analysis of beams, plates, and shells: this extension requires the introduction of rotational DOFs. This can be done, for instance, by using Hermite polynomial shape functions, as recently proposed for 2D and 3D Kirchhoff beams by Armero [62, 63];

– application to form finding and structural optimisation problems: to this aim, the formulation by Pauletti et al. [34–37] could be enhanced with the introduction of specific constitutive laws;

– application to structural dynamics: in this direction, a first study has been conducted on the dynamic simulation of deployable cable nets for space applications [64];

– extension to rate-dependent material models, such as elastoplasticity, viscoplasticity, and viscoelasticity: to this aim, an objective stress rate shall be introduced, e.g. the Jaumann rate. The interested reader can find further details on this topic in the books by Wriggers [2], Bonet et al. [13], and Simo and Hughes [65].

Appendix A: Displacement-based FE formulation

In the DFEF, the Green–Lagrange strain is calculated based on the nodal displacements. To this aim, the nodal displacement vector of an element, $\mathbf{u}_e = \mathbf{x}_e - \bar{\mathbf{x}}_e$ can be substituted into Eq. (11), which becomes

$$E_{\alpha\beta} = \left(\bar{\mathbf{x}}_e + \frac{1}{2} \mathbf{u}_e \right)^{\mathsf{T}} \Gamma_{\alpha\beta} \mathbf{u}_e. \tag{84}$$

The strain components can be collected into a column vector,

$$\mathbf{e} = \left\{ \begin{array}{c} E_{11} \\ \vdots \\ E_{d_e d_e} \end{array} \right\}, \tag{85}$$

and expressed in terms of the nodal displacements as follows:

$$\mathbf{e} = \mathbf{B}(\mathbf{u}_e) \, \mathbf{u}_e, \tag{86}$$

where

$$\mathbf{B}(\mathbf{u}_e) = \mathbf{B}_0 + \mathbf{B}_1(\mathbf{u}_e), \tag{87}$$

is the strain–displacement matrix. It is the sum of a constant part,

$$\mathbf{B}_0 = \begin{bmatrix} \bar{\mathbf{x}}_e^{\mathsf{T}} \Gamma_{11} \\ \vdots \\ \bar{\mathbf{x}}_e^{\mathsf{T}} \Gamma_{d_e d_e} \end{bmatrix}, \tag{88}$$

and a part depending linearly on $\mathbf{u}_e$,

$$\mathbf{B}_1(\mathbf{u}_e) = \frac{1}{2} \begin{bmatrix} \mathbf{u}_e^{\mathsf{T}} \Gamma_{11} \\ \vdots \\ \mathbf{u}_e^{\mathsf{T}} \Gamma_{d_e d_e} \end{bmatrix}. \tag{89}$$

If a linear constitutive law is assumed (according to the SVK material model), then the second Piola–Kirchhoff stresses can be expressed as follows:

$$S_{\alpha\beta} = \sum_{\gamma=1}^{d_e} \sum_{\delta=1}^{d_e} C_{\alpha\beta\gamma\delta} E_{\gamma\delta}, \tag{90}$$

where $C_{\alpha\beta\gamma\delta}$ are the fourth-order material elasticity tensor components. Then, by substituting Eqs. (84) and (90) into Eqs. (32) and (33), the elastic force vector of the element is obtained as a function of the nodal displacement vector:

$$\mathbf{f}_e(\mathbf{u}_e) = \hat{\mathbf{K}}_e(\mathbf{u}_e) \, \mathbf{u}_e, \tag{91}$$

where

$$\hat{\mathbf{K}}_e(\mathbf{u}_e) = \int_{\bar{\Omega}_e} \sum_{\alpha=1}^{d_e} \sum_{\beta=1}^{d_e} \sum_{\gamma=1}^{d_e} \sum_{\delta=1}^{d_e} C_{\alpha\beta\gamma\delta} \cdot$$
$$\Gamma_{\alpha\beta} \left(\bar{\mathbf{x}}_e + \mathbf{u}_e \right) \left(\bar{\mathbf{x}}_e + \frac{1}{2} \mathbf{u}_e \right)^{\mathsf{T}} \Gamma_{\gamma\delta} \, \mathrm{d}\bar{V}_e \tag{92}$$

is the secant stiffness matrix of the element. Matrix $\hat{\mathbf{K}}_e$ is not symmetric, but can be replaced by a symmetric matrix as explained below.

By substituting Eq. (92) into (91) and rearranging the terms depending on $\bar{\mathbf{x}}_e$ and $\mathbf{u}_e$, the elastic force vector of the element can be expressed as

$$\mathbf{f}_e(\mathbf{u}_e) = \mathbf{K}_e(\mathbf{u}_e) \, \mathbf{u}_e, \tag{93}$$

where

$$\mathbf{K}_e(\mathbf{u}_e) = \mathbf{K}_0^e + \mathbf{K}_1^e(\mathbf{u}_e) + \mathbf{K}_2^e(\mathbf{u}_e) \tag{94}$$

is a symmetric secant stiffness matrix. In Eq. (94), the following three contributions appear: a constant term,

$$\mathbf{K}_0^e = \int_{\bar{\Omega}_e} \sum_{\alpha=1}^{d_e} \sum_{\beta=1}^{d_e} \sum_{\gamma=1}^{d_e} \sum_{\delta=1}^{d_e} C_{\alpha\beta\gamma\delta} \Gamma_{\alpha\beta} \bar{\mathbf{x}}_e \bar{\mathbf{x}}_e^{\mathsf{T}} \Gamma_{\gamma\delta} \, \mathrm{d}\bar{V}_e, \qquad (95)$$

which corresponds to the stiffness matrix used in linear analysis; a linear term in $\mathbf{u}_e$,

$$\mathbf{K}_1^e (\mathbf{u}_e) = \frac{1}{2} \int_{\bar{\Omega}_e} \sum_{\alpha=1}^{d_e} \sum_{\beta=1}^{d_e} \sum_{\gamma=1}^{d_e} \sum_{\delta=1}^{d_e} C_{\alpha\beta\gamma\delta} \cdot$$
$$\Gamma_{\alpha\beta} \left[\left(\bar{\mathbf{x}}_e \mathbf{u}_e^{\mathsf{T}} + \mathbf{u}_e \bar{\mathbf{x}}_e^{\mathsf{T}} \right) \Gamma_{\gamma\delta} + \left(\bar{\mathbf{x}}_e^{\mathsf{T}} \Gamma_{\gamma\delta} \mathbf{u}_e \right) \mathbf{I} \right] \mathrm{d}\bar{V}_e; \qquad (96)$$

and a quadratic term in $\mathbf{u}_e$,

$$\mathbf{K}_2^e (\mathbf{u}_e) = \frac{1}{2} \int_{\bar{\Omega}_e} \sum_{\alpha=1}^{d_e} \sum_{\beta=1}^{d_e} \sum_{\gamma=1}^{d_e} \sum_{\delta=1}^{d_e} C_{\alpha\beta\gamma\delta} \cdot$$
$$\Gamma_{\alpha\beta} \mathbf{u}_e \mathbf{u}_e^{\mathsf{T}} \Gamma_{\gamma\delta} \, \mathrm{d}\bar{V}_e. \qquad (97)$$

Unfortunately, the above procedure cannot be applied in general for arbitrary nonlinear hyperelastic materials.

Appendix B: Kinematic restraints

If the system is subject to kinematic restraints in the form of imposed nodal displacements, these can be incorporated into the governing equations as explained in the following.

Let $\rho \in \mathbb{R}^N$ be a vector, whose generic component

$$\rho_I = \begin{cases} 1, & \text{if the } I\text{-th DOF is restrained,} \\ 0, & \text{otherwise,} \end{cases} \qquad (98)$$

with $I = 1, \ldots, N$. Besides, let $\mathbf{P} = \mathrm{diag}(\rho_1, \ldots, \rho_N) \in \mathbb{R}^{N \times N}$ be a matrix having the components of ρ on its main diagonal.

The kinematic restraints can be described by the following equations:

$$\mathbf{P}\mathbf{x} = \mathbf{P}(\bar{\mathbf{x}} + \bar{\mathbf{u}}), \qquad (99)$$

where $\bar{\mathbf{u}} \in \mathbb{R}^N$ is a vector of imposed (not necessarily null) nodal displacements. It should be noted that because of multiplication by matrix $\mathbf{P}$, only imposed displacements corresponding to restrained DOFs will be effective.

The governing static equilibrium equations can be deduced from the stationarity of the total potential energy Eq. (22) subject to restraint Eqs. (99). To this aim, the method of Lagrange

multipliers can be exploited. Let us consider the Lagrangian function

$$\mathcal{L}(\mathbf{x}, \boldsymbol{\mu}) = \mathcal{V}(\mathbf{x}) - \boldsymbol{\mu}^{\mathsf{T}} \mathbf{P}(\mathbf{x} - \bar{\mathbf{x}} - \bar{\mathbf{u}}), \qquad (100)$$

where $\boldsymbol{\mu} \in \mathbb{R}^N$ is a vector of Lagrange multipliers. The stationarity of the Lagrangian function Eq. (100) is imposed by setting to zero its derivatives with respect to $\mathbf{x}$,

$$\mathbf{g}(\mathbf{x}) = \frac{\partial \mathcal{L}}{\partial \mathbf{x}} = \mathbf{S}(\mathbf{x})\mathbf{x} - \mathbf{p} - \mathbf{r} = \mathbf{0}, \qquad (101)$$

and $\boldsymbol{\mu}$,

$$\mathbf{h}(\mathbf{x}) = \frac{\partial \mathcal{L}}{\partial \boldsymbol{\mu}} = -\mathbf{P}(\mathbf{x} - \bar{\mathbf{x}} - \bar{\mathbf{u}}) = \mathbf{0}. \qquad (102)$$

Equations (101) represent the static equilibrium equations for a system with kinematic restraints. Here,

$$\mathbf{r} = \mathbf{P}\boldsymbol{\mu} \qquad (103)$$

is the vector of nodal restraint reactions. Because of multiplication by matrix $\mathbf{P}$, non-zero reactions can occur only at restrained DOFs. Besides, it is easy to recognise that Eqs. (102) are equivalent to the kinematic restraint Eqs. (99).

To solve the problem, it is convenient to introduce Eqs. (102) into (101) in place of the equations containing the unknown restraint reactions. As a result, the following static-kinematic governing equations are obtained:

$$\mathbf{g}^*(\mathbf{x}) = \mathbf{S}^*(\mathbf{x})\mathbf{x} - \mathbf{p}^* = \mathbf{0}, \qquad (104)$$

where the modified secant stiffness matrix,

$$\mathbf{S}^*(\mathbf{x}) = (\mathbf{I} - \mathbf{P})\mathbf{S}(\mathbf{x})(\mathbf{I} - \mathbf{P}) + \mathbf{P}, \qquad (105)$$

and modified load vector,

$$\mathbf{p}^* = (\mathbf{I} - \mathbf{P})\mathbf{p} + [\mathbf{I} - (\mathbf{I} - \mathbf{P})\mathbf{S}(\mathbf{x})]\mathbf{P}(\bar{\mathbf{x}} + \bar{\mathbf{u}}), \qquad (106)$$

have been defined. In Eqs. (105) and (106), $\mathbf{I} \in \mathbb{R}^{N \times N}$ is the identity matrix.

Appendix C: Constitutive laws

C.1 Stress–strain relationships

For each assumed material model, the specific expressions of the second Piola–Kirchhoff stress tensor, $\mathbf{S}$, can be obtained by suitably differentiating the strain energy density function, $\bar{\varphi}$, with respect to the Green–Lagrange strain tensor, $\mathbf{E}$, according to Eq. (21). Thus, after some manipulations

and simplifications (for further details, see also [13]), from Eqs. (81) and (82), the following stress–strain relationships are obtained for the SVK material,

$$\mathbf{S} = \lambda I_1^E \mathbf{I} + 2\mu \mathbf{E}, \tag{107}$$

and the NH material,

$$\mathbf{S} = \frac{1}{2}\lambda \left(I_3^C - 1 \right) \mathbf{C}^{-1} + \mu \left(\mathbf{I} - \mathbf{C}^{-1} \right). \tag{108}$$

In the principal strain reference system, the stress–strain relationships become as follows for the SVK material,

$$S_\alpha = \lambda \left(E_I + E_{II} + E_{III} \right) + 2\mu E_\alpha, \tag{109}$$

and the NH material,

$$S_\alpha = \frac{1}{2}\lambda \left(C_I C_{II} C_{III} - 1 \right) \frac{1}{C_\alpha} + \mu \left(1 - \frac{1}{C_\alpha} \right), \tag{110}$$

where E_α and C_α denote the principal values (eigenvalues) of tensors $\mathbf{E}$ and $\mathbf{C}$, respectively, with $\alpha \in \{I, II, III\}$.

C.2 Truss bar element

The truss bar element is assumed to be in a uniaxial stress state with the first principal direction, I, coincident with the axial direction and the other two principal directions, II and III, lying in the cross-section plane. Thus, by substituting $S_{II} = S_{III} = 0$ into Eqs. (109) and (110), the principal strains in the cross-section plane are obtained. Then, the axial component of the second Piola–Kirchhoff stress, $S_{11} = S_I$, turns out to be

$$S_{11} = E E_I = E E_{11} \tag{111}$$

for the SVK material and

$$S_{11} = \mu \left(1 + \frac{\mu/\lambda}{C_I^2} - \sqrt{\frac{1 + 2\mu/\lambda}{C_I^3} + \frac{(\mu/\lambda)^2}{C_I^4}} \right), \tag{112}$$

with $C_I = 2E_I + 1 = 2E_{11} + 1$, for the NH material. It is worth noting that, for incompressible materials, $\lambda \to +\infty$ and the latter equation simplifies to

$$S_{11} = \mu \left(1 - \frac{1}{C_I^{3/2}} \right). \tag{113}$$

According to Eqn. (59), the tangent elastic modulus is

$$C_{1111} = E \tag{114}$$

for the SVK material and

$$C_{1111} = \frac{\mu}{C_I^3} \left[\frac{4\,(\mu/\lambda)^2 + 3\,(1 + 2\mu/\lambda)\,C_I}{\sqrt{(\mu/\lambda)^2 + (1 + 2\mu/\lambda)\,C_I}} - 4\mu/\lambda \right] \tag{115}$$

for the NH material. For incompressible materials, the latter equation reduces to

$$C_{1111} = 3\mu \frac{1}{C_I^{5/2}}. \tag{116}$$

C.3 Plane triangular element

The triangular element is assumed to be in a plane stress state with null stress along the third principal direction, III, normal to the element mid-plane. By substituting $S_{III} = 0$ into Eqs. (109) and (110), the principal strain in the same direction is calculated. Then, the components are detemined of the second Piola–Kirchhoff stress along the in-plane principal directions, I and II:

$$S_I = \frac{E}{1 - \nu^2} \left(E_I + \nu E_{II} \right), \tag{117}$$

$$S_{II} = \frac{E}{1 - \nu^2} \left(\nu E_I + E_{II} \right), \tag{118}$$

for the SVK material and

$$S_I = \mu \left(1 - \frac{1}{C_I} \frac{1 + 2\mu/\lambda}{C_I C_{II} + 2\mu/\lambda} \right), \tag{119}$$

$$S_{II} = \mu \left(1 - \frac{1}{C_{II}} \frac{1 + 2\mu/\lambda}{C_I C_{II} + 2\mu/\lambda} \right), \tag{120}$$

with $C_I = 2E_I + 1$ and $C_{II} = 2E_{II} + 1$, for the NH material. For incompressible materials, the latter expressions reduce to

$$S_I = \mu \left(1 - \frac{1}{C_I^2 C_{II}} \right), \tag{121}$$

$$S_{II} = \mu \left(1 - \frac{1}{C_I C_{II}^2} \right). \tag{122}$$

The stress components in the local reference system of the element can be obtained from a suitable rotation as follows:

$$S_{11} = \frac{S_I + S_{II}}{2} + \frac{S_I - S_{II}}{2} \cos 2\theta_I, \tag{123}$$

$$S_{22} = \frac{S_I + S_{II}}{2} - \frac{S_I - S_{II}}{2} \cos 2\theta_I, \tag{124}$$

$$S_{12} = \frac{S_I - S_{II}}{2} \sin 2\theta_I, \tag{125}$$

where θ_I is the angle between the local $\bar{s}_1$-axis and the first principal direction, I, as computed from the following equation:

$$\tan 2\theta_I = \frac{2E_{12}}{E_{11} - E_{22}}, \tag{126}$$

where E_{11}, E_{22}, and E_{12} are the components of the Green–Lagrange strain tensor in the local reference system. In the FE implementation, such components are calculated from Eqn. (11) with Eqns. (75)–(77). Then, E_I and E_{II} are obtained from a suitable rotation of the tensor.

Lastly, the components of the material elasticity tensor Eqn. (80) in the local reference system are computed from the derivatives of the stresses in the principal strain directions by applying a suitable rotation as follows [13]:

$$C_{1111} = c^4 \frac{\partial S_I}{\partial E_I} + c^2 s^2 \left(\frac{\partial S_I}{\partial E_{II}} + \frac{\partial S_{II}}{\partial E_I} \right) + s^4 \frac{\partial S_{II}}{\partial E_{II}} \\ + 2c^2 s^2 \frac{\Delta S}{\Delta E}, \tag{127}$$

$$C_{1112} = c^3 s \left(\frac{\partial S_I}{\partial E_I} - \frac{\partial S_I}{\partial E_{II}} \right) + c s^3 \left(\frac{\partial S_{II}}{\partial E_I} - \frac{\partial S_{II}}{\partial E_{II}} \right) \\ - cs \left(c^2 - s^2 \right) \frac{\Delta S}{\Delta E}, \tag{128}$$

$$C_{1122} = c^2 s^2 \frac{\partial S_I}{\partial E_I} + c^4 \frac{\partial S_I}{\partial E_{II}} + s^4 \frac{\partial S_{II}}{\partial E_I} + c^2 s^2 \frac{\partial S_{II}}{\partial E_{II}} \\ - 2c^2 s^2 \frac{\Delta S}{\Delta E}, \tag{129}$$

$$C_{1212} = c^2 s^2 \left(\frac{\partial S_I}{\partial E_I} - \frac{\partial S_I}{\partial E_{II}} - \frac{\partial S_{II}}{\partial E_I} + \frac{\partial S_{II}}{\partial E_{II}} \right) \\ + \frac{1}{2} \left(c^2 - s^2 \right)^2 \frac{\Delta S}{\Delta E}, \tag{130}$$

$$C_{1222} = cs \left(s^2 \frac{\partial S_I}{\partial E_I} + c^2 \frac{\partial S_I}{\partial E_{II}} - s^2 \frac{\partial S_{II}}{\partial E_I} - c^2 \frac{\partial S_{II}}{\partial E_{II}} \right) \\ + cs \left(c^2 - s^2 \right) \frac{\Delta S}{\Delta E}, \tag{131}$$

$$C_{2222} = s^4 \frac{\partial S_I}{\partial E_I} + c^2 s^2 \left(\frac{\partial S_I}{\partial E_{II}} + \frac{\partial S_{II}}{\partial E_I} \right) + c^4 \frac{\partial S_{II}}{\partial E_{II}} \\ + 2c^2 s^2 \frac{\Delta S}{\Delta E}, \tag{132}$$

where $c = \cos\theta_I$, $s = \sin\theta_I$, and

$$\frac{\Delta S}{\Delta E} = \frac{S_I - S_{II}}{E_I - E_{II}}. \tag{133}$$

References

1. Zienkiewicz OC, Taylor RL, Fox DD (2014) The finite element method for solid and structural mechanics—seventh edition. Elsevier, Amsterdam . https://doi.org/10.1016/C2009-0-26332-X
2. Wriggers P (2008) Nonlinear finite element methods. Springer, Berlin (2008).https://doi.org/10.1007/978-3-540-71001-1
3. Kim NH (2015) Introduction to nonlinear finite element analysis. Springer, New York .https://doi.org/10.1007/978-1-4419-1746-1
4. Felippa CA, Crivelli LA, Haugen B (1994) A survey of the core-congruential formulation for geometrically nonlinear TL finite elements. Arch Comput Methods Eng 1(1):1–48. https://doi.org/10.1007/BF02736179
5. Oñate E (1995) On the derivation and possibilities of the secant stiffness matrix for non linear finite element analysis. Comput Mech 15(6):572–593. https://doi.org/10.1007/BF00350269
6. Morán A, Oñate E, Miquel J (1998) A general procedure for deriving symmetric expressions for the secant and tangent stiffness matrices in finite element analysis. Int J Numer Methods Eng 42(2):219–236
7. Pedersen P (2005) Analytical stiffness matrices with Green–Lagrange strain measure. Int J Numer Methods Eng 62(3):334–352. https://doi.org/10.1002/nme.1174
8. Pedersen P (2006) Analytical stiffness matrices for tetrahedral elements. Comput Methods Appl Mech Eng 196(1–3):261–278. https://doi.org/10.1016/j.cma.2006.04.001
9. Gülümser E, Güdükbay U, Filiz S (2014) Fast stiffness matrix calculation for nonlinear finite element method. J Appl Math 2014(932314):1–12. https://doi.org/10.1155/2014/932314
10. Valvo PS (2022) Derivation of symmetric secant stiffness matrices for nonlinear finite element analysis. Adv Sci Technol Res J 16(6):118–125. https://doi.org/10.12913/22998624/155942
11. Bonet J (1994) The incremental flow formulation for the numerical analysis of plane stress and thin sheet viscous forming processes. Comput Methods Appl Mech Eng 114(1–2):103–122. https://doi.org/10.1016/0045-7825(94)90164-3
12. Bonet J, Wood RD, Mahaney J, Heywood P (2000) Finite element analysis of air supported membrane structures. Comput Methods Appl Mech Eng 190(5–7):579–595. https://doi.org/10.1016/S0045-7825(99)00428-4
13. Bonet J, Gil AJ, Wood RD (2016) Nonlinear solid mechanics for finite element analysis: statics. Cambridge University Press, Cambridge . https://doi.org/10.1017/CBO9781316336144
14. Bonet J, Gil AJ, Wood RD(2021) Nonlinear solid mechanics for finite element analysis: dynamics. Cambridge University Press, Cambridge . https://doi.org/10.1017/9781316336083
15. Coda HB, Greco M (2004) A simple FEM formulation for large deflection 2D frame analysis based on position description. Comput Methods Appl Mech Eng 193(33–35):3541–3557. https://doi.org/10.1016/j.cma.2004.01.005
16. Greco M, Gesualdo FAR, Venturini WS, Coda HB (2006) Nonlinear positional formulation for space truss analysis. Finite Elem

Anal Des 42(12):1079–1086. https://doi.org/10.1016/j.finel.2006.04.007

17. Greco M, Coda HB (2006) Positional FEM formulation for flexible multi-body dynamic analysis. J Sound Vib 290(3–5):1141–1174. https://doi.org/10.1016/j.jsv.2005.05.018

18. Coda HB, Paccola RR (2007) An alternative positional FEM formulation for geometrically non-linear analysis of shells: curved triangular isoparametric elements. Comput Mech 40(1):185–200. https://doi.org/10.1007/s00466-006-0094-1

19. Pascon JP, Coda HB (2013) Large deformation analysis of elasto-plastic homogeneous materials via high order tetrahedral finite elements. Finite Elem Anal Des 76:21–38. https://doi.org/10.1016/j.finel.2013.08.006

20. Avancini G, Sanches RAK (2020) A total Lagrangian position-based finite element formulation for free-surface incompressible flows. Finite Elem Anal Des 169(103348):1–17. https://doi.org/10.1016/j.finel.2019.103348

21. Coda HB, Sanches RAK, Paccola RR (2022) Alternative multiscale material and structures modeling by the finite-element method. Eng Comput 38(Suppl 1):S311–S329. https://doi.org/10.1007/s00366-020-01148-y

22. Shabana AA (1997) Definition of the slopes and the finite element absolute nodal coordinate formulation. Multibody SysDyn 1(3):339–348. https://doi.org/10.1023/A:1009740800463

23. Shabana AA (1998) Computer implementation of the absolute nodal coordinate formulation for flexible multibody dynamics. Nonlinear Dyn 16(3):293–306. https://doi.org/10.1023/A:1008072517368

24. Dmitrochenko O, Mikkola A (2008) Two simple triangular plate elements based on the absolute nodal coordinate formulation. J Comput Nonlinear Dyn 3(4):1–8. https://doi.org/10.1115/1.2960479

25. Olshevskiy A, Dmitrochenko O, Dai MD, Kim CW (2015) The simplest 3-, 6- and 8-noded fully-parameterized ANCF plate elements using only transverse slopes. Multibody SysDyn 34(1):23–51. https://doi.org/10.1007/s11044-014-9411-1

26. Pappalardo CM, Wang T, Shabana AA (2017) On the formulation of the planar ANCF triangular finite elements. Nonlinear Dyn 89(2):1019–1045. https://doi.org/10.1007/s11071-017-3498-x

27. Lan P, Wang T, Yu Z (2019) A new planar triangular element based on the absolute nodal coordinate formulation. Proc Inst Mech Eng Part K: J Multi-body Dyn 233(1):163–173. https://doi.org/10.1177/146441931877

28. Maqueda LG, Shabana AA (2007) Poisson modes and general nonlinear constitutive models in the large displacement analysis of beams. Multibody SysDyn 18(3):375–396. https://doi.org/10.1007/s11044-007-9077-z

29. Orzechowski G (2015) Frą czeks J. Nearly incompressible nonlinear material models in the large deformation analysis of beams using ANCF. Nonlinear Dyn 82(1–2):451–464. https://doi.org/10.1007/s11071-015-2167-1

30. Obrezkov LP, Matikainen MK, Harish AB (2020) A finite element for soft tissue deformation based on the absolute nodal coordinate formulation. Acta Mech 231(4):1519–1538. https://doi.org/10.1007/s00707-019-02607-4

31. Li L, Wang Y, Guo Y, Zhang D (2023) Large deformations of hyperelastic curved beams based on the absolute nodal coordinate formulation. Nonlinear Dyn 111:4191–4204. https://doi.org/10.1007/s11071-022-08076-0

32. Luo K, Liu C, Tian Q, Hu H (2016) Nonlinear static and dynamic analysis of hyper-elastic thin shells via the absolute nodal coordinate formulation. Nonlinear Dyn 85(2):949–971. https://doi.org/10.1007/s11071-016-2735-z

33. García-Vallejo D, Mayo J, Escalona JL, Domínguez J (2004) Efficient evaluation of the elastic forces and the Jacobian in the absolute nodal coordinate formulation. Nonlinear Dyn 35(4):313–329. https://doi.org/10.1023/B:NODY.0000027747.41604.20

34. Pauletti RMO (2006) An extension of the force density procedure to membrane structures. In: Proceedings of the IASS symposium/APCS conference—new olympics, new shell and spatial structures, Beijing

35. Pauletti RMO, Pimenta PM (2008) The natural force density method for the shape finding of taut structures. Comput Methods Appl Mech Eng 197(49–50):4419–4428. https://doi.org/10.1016/j.cma.2008.05.017

36. Pauletti RMO, Fernandes FL (2020) An outline of the natural force density method and its extension to quadrilateral elements. Int J Solids Struct 185–186:423–438. https://doi.org/10.1016/j.ijsolstr.2019.09.003

37. Pauletti RMO, Arcaro VF (2024) An extension of the natural force density method to 3D problems. Arch Appl Mech. https://doi.org/10.1007/s00419-024-02580-y

38. Kuna M. Finite elements in fracture mechanics. Springer, Dordrecht (2013). https://doi.org/10.1007/978-94-007-6680-8

39. Ogden RW (1984) Non-linear elastic deformations. Ellis Harwood, Chichester

40. Penrose R (1955) A generalized inverse for matrices. Proc Camb Philos Soc 51(3):406–413. https://doi.org/10.1017/S0305004100030401

41. Bažant ZP, Cedolin L (1991) Stability of structures. Oxford University Press, New York

42. Schröder J, Wick T, Reese S et al (2021) A selection of benchmark problems in solid mechanics and applied mathematics. Arch Comput Methods Eng 28:713–751. https://doi.org/10.1007/s11831-020-09477-3

43. von Mises R (1923) Über die Stabilitätsprobleme der Elastizitätstheorie. Z Angew Math Mech 3:406–422. https://doi.org/10.1002/zamm.19230030602

44. von Mises R, Ratzersdorfer J (1925) Die Knicksicherheit von Fachwerken. Z Angew Math Mech 5:218–235. https://doi.org/10.1002/zamm.19250050305

45. Pecknold DA, Ghaboussi J, Healey TJ (1985) Snap-through and bifurcation in a simple structure. ASCE J Eng Mech 111(7):909–922. https://doi.org/10.1061/(ASCE)0733-9399(1985)111:7(909)

46. Ligarò S, Valvo P (1999) A self-adaptive strategy for uniformly accurate tracing of the equilibrium paths of elastic reticulated structures. Int J Numer Methods Eng 46(6):783–804. https://doi.org/10.1002/(SICI)1097-0207(19991030)46:6%3C783::AID-NME674%3E3.0.CO;2-G

47. Pelliciari M, Tarantino AM (2020) Equilibrium paths for von Mises trusses in finite elasticity. J Elast 138(2):145–168. https://doi.org/10.1007/s10659-019-09731-1

48. Fonseca FM, Gonçalves PB (2022) Nonlinear behavior and instabilities of a hyperelastic Von Mises truss. Int J Non-Linear Mech 142:103964. https://doi.org/10.1016/j.ijnonlinmec.2022.103964

49. Pelliciari M, Falope FO, Lanzoni L, Tarantino AM (2023) Theoretical and experimental analysis of the von Mises truss subjected to a horizontal load using a new hyperelastic model with hardening. Eur J Mech/A Solids 97:104825. https://doi.org/10.1016/j.euromechsol.2022.104825

50. Dao NT, Thu TVT (2024) Hybrid finite element method in nonlinear dynamic analysis of trusses. Int J Struct Stab Dyn, 2450195. https://doi.org/10.1142/S0219455424501955

51. Riks E (1979) An incremental approach to the solution of snapping and buckling problems. Int J Solids Struct 15(7):529–551. https://doi.org/10.1016/0020-7683(79)90081-7

52. Crisfield MA (1981) A fast incremental/iterative solution procedure that handles snap-through. Comput Struct 13(1–3):55–62. https://doi.org/10.1016/0045-7949(81)90108-5

53. Cook RD, Al-Abdulla JK (1969) Some plane quadrilateral hydrid finite elements. AIAA J 7(11):2184–2185. https://doi.org/10.2514/3.5594

54. Cook RD (1974) Improved two-dimensional finite element. J Struct Div 100(9):1851–1863. https://doi.org/10.1061/JSDEAG.0003877

55. The MathWorks Inc (2022) MATLAB version: 9.13.0 (R2022b), Natick, Massachusetts: The MathWorks Inc. https://www.mathworks.com

56. Düster A, Hartmann S, Rank E (2003) p-FEM applied to finite isotropic hyperelastic bodies. Comput Methods Appl Mech Eng 192(47–48):5147–5166. https://doi.org/10.1016/j.cma.2003.07.003

57. Pascon JP (2019) Large deformation analysis of plane-stress hyperelastic problems via triangular membrane finite elements. Int J Adv Struct Eng 11:331–350. https://doi.org/10.1007/s40091-019-00234-w

58. Brezzi F, Fortin M (1991) Mixed and hybrid finite element methods. Springer, New York . https://doi.org/10.1007/978-1-4612-3172-1_6

59. Jones MT, Patrick ML (1993) Bunch–Kaufman factorization for real symmetric indefinite banded matrices. SIAM J Matrix Anal Appl 14(2):553–559. https://doi.org/10.1137/0614039

60. Alberini R, Spagnoli A, Terzano M (2021) Numerical modelling of wrinkled hyperelastic membranes with topologically complex internal boundary conditions. Int J Mech Sci 212:106816. https://doi.org/10.1016/j.ijmecsci.2021.106816

61. Firouzi N, Żur KK (2023) On the generalized nonlinear mechanics of compressible, incompressible, isotropic, and anisotropic hyperelastic membranes. Int J Solids Struct 264:112088. https://doi.org/10.1016/j.ijsolstr.2022.112088

62. Armero F (2024) A new Hermite finite element for nonlinear Kirchhoff rods: the plane case. Int J Numer Meth Eng 125(12):e7448. https://doi.org/10.1002/nme.7448

63. Armero F (2024) A finite element for nonlinear three-dimensional Kirchhoff rods. Comput Struct 299:107393. https://doi.org/10.1016/j.compstruc.2024.107393

64. Fisicaro P, Pasini A, Valvo PS (2022) Simulation of deployable cable nets for active debris removal in space. J Phys: Conf Ser 2412(1):012010. https://doi.org/10.1088/1742-6596/2412/1/012010

65. Simo JC, Hughes TJR (1998) Computational inelasticity. Springer, New York . https://doi.org/10.1007/b98904